



## Differential Exhumation Across the Longriba Fault System: Implications for the Eastern Tibetan Plateau

Claire Ansberque, Vincent Godard, Valerio Olivetti, Olivier Bellier, Julia de Sigoyer, Matthias Bernet, Konstanze Stübner, Xibin Tan, Xiwei Xu, Todd Ehlers

### ► To cite this version:

Claire Ansberque, Vincent Godard, Valerio Olivetti, Olivier Bellier, Julia de Sigoyer, et al.. Differential Exhumation Across the Longriba Fault System: Implications for the Eastern Tibetan Plateau. *Tectonics*, 2018, 37 (2), pp.663 - 679. 10.1002/2017TC004816 . hal-01791792

**HAL Id: hal-01791792**

**<https://amu.hal.science/hal-01791792>**

Submitted on 26 Apr 2019

**HAL** is a multi-disciplinary open access archive for the deposit and dissemination of scientific research documents, whether they are published or not. The documents may come from teaching and research institutions in France or abroad, or from public or private research centers.

L'archive ouverte pluridisciplinaire **HAL**, est destinée au dépôt et à la diffusion de documents scientifiques de niveau recherche, publiés ou non, émanant des établissements d'enseignement et de recherche français ou étrangers, des laboratoires publics ou privés.

# Differential Exhumation Across the Longriba Fault System: Implications for the Eastern Tibetan Plateau

Claire Ansberque<sup>1,2</sup>, Vincent Godard<sup>1</sup>, Valerio Olivetti<sup>1</sup>, Olivier Bellier<sup>1</sup>, Julia de Sigoyer<sup>3</sup>, Matthias Bernet<sup>3</sup>, Konstanze Stübner<sup>4</sup>, Xibin Tan<sup>5</sup>, Xiwei Xu<sup>5</sup>, and Todd A. Ehlers<sup>4</sup>

1 Aix-Marseille Univ, CNRS, IRD INRA, Coll France, CEREGE, Aix en Provence, France, 2 Department of Geology, Trinity College Dublin, Museum Building, College Green, Dublin 2, Ireland, 3 Grenoble Alpes Université, CNRS, UMR 5275, ISTerre, Grenoble, France, 4 Department of Geosciences, University of Tübingen, Tübingen, Germany, 5 Institute of Geology, China Earthquake Administration, Beijing, China

Citation: Ansberque, C., Godard, V., Olivetti, V., Bellier, O., de Sigoyer, J., Bernet, M., et al. (2018). Differential exhumation across the Longriba Fault system: Implications for the eastern Tibetan Plateau. *Tectonics*, 37. <https://doi.org/10.1002/2017TC004816>

## Abstract

The deformation processes at work across the eastern margin of the Tibetan Plateau remain controversial. The interpretation of its tectonic history is often polarized between two deformation models: ductile flow in the lower crust and shortening and crustal thickening accommodated by brittle structures in the upper crust. Many geological investigations on this plateau margin focused on the Longmen Shan, at the western edge of the Sichuan Basin. However, the Longriba fault system (LFS) located 200 km northwest and parallel to the Longmen Shan structures provides an opportunity to understand the role of hinterland faults in eastern Tibet geodynamics. For this reason, we investigate the exhumation history of rocks across the LFS using (U-Th)/He and fission track ages from apatite and zircon. Results show a significant contrast in cooling histories across the Maoergai fault, the southernmost fault of the LFS. South of the Maoergai fault, the bedrock records a rapid increase in exhumation rate since ~10–15 Ma. In contrast, the area north of the fault has experienced steady cooling since ~25–35 Ma. We attribute this cooling contrast to ~2 km of differential rock uplift across the Maoergai fault, providing the first evidence of activity of the LFS in the Late Cenozoic. Our results indicate that deformation of the eastern Tibetan margin has been partitioned into the LFS and the Longmen Shan over an ~200 km wide block, which should be incorporated in future studies on the region's deformation, and in both above-mentioned deformation models.

## 1. Introduction

The geodynamic processes responsible for the development of large orogenic plateaus such as Tibet are actively debated (e.g., Royden et al., 2008; Tapponnier et al., 2001). In recent decades, plateau margins have attracted attention because the understanding of their dynamics and history provides insights into the modes of crustal deformation responsible for the plateau structure and morphology and more widely into the deformation of continental lithosphere (e.g., Clark, House, et al., 2005; Medvedev & Beaumont, 2006; Thiede & Ehlers, 2013; Royden et al., 1997; Vanderhaeghe et al., 2003). The eastern Tibetan margin represents one of the steepest topographic gradients on Earth with elevations ranging from 500 m above sea level (asl) in the Sichuan basin to 4500 masl in the Longmen Shan over a horizontal distance of ~30 km (Figure 1a). Yet the estimated shortening rates across the margin over geodetic timescales (<3 mm/yr; Shen et al., 2009) is not consistent with this significant topographic signal. Due to these apparently conflicting observations, the eastern Tibetan margin has been a priority target for investigations related to orogenic processes (Airaghi et al., 2017; Burchfiel et al., 1995; Clark & Royden, 2000; Clark, House, et al., 2005; Guo et al., 2013; Hubbard & Shaw, 2009; Kirby et al., 2002; Royden et al., 2008; Robert et al., 2009; Tian et al., 2013; 2016), active continental deformation (Burchfiel et al., 2008; Densmore et al., 2007; De Michele et al., 2010; Feng et al., 2016; Kirby et al., 2000; Qi et al., 2011; Ren et al., 2013a; Shen et al., 2009; Wang et al., 2012; Xu et al., 2008), and interactions between tectonics and surface processes (Ansberque et al., 2015; Clark, House, et al., 2005; Godard et al., 2010; Kirby et al., 2003; Liu-Zeng et al., 2011; Ouimet et al., 2009, 2010; Parker et al.,

2011; Tian et al., 2015; Wang et al., 2017). Different models of lithospheric deformation have been proposed to explain the development of the eastern Tibetan margin. For example, ductile and inflating flow of the lower crust driving a broad regional uplift of the margin, referred to as channel flow model (e.g., Clark & Royden, 2000; Royden et al., 1997), may have occurred at ~10–12 Ma (Clark, House, et al., 2005; Ouimet et al., 2010; Wang et al., 2012). Alternatively, lithospheric thickening may result from brittle crustal shortening accommodated by crustal-scale thrusting largely confined to the Longmen Shan (e.g., Hubbard & Shaw, 2009; Liu-Zeng et al., 2009; Tian et al., 2013). The channel flow model has gained particular attention, as it reconciles the high-elevation low relief of the eastern Tibetan plateau terminated by an abrupt margin (Royden et al., 2008) with the slow convergence rate and the slow deformation of the main structures of the Longmen Shan (Burchfiel et al., 2008; Clark & Royden, 2000; Royden et al., 1997). The presence of low-velocity/low-resistivity zones in the crust below eastern Tibet documented by several seismic and magnetotelluric surveys has been interpreted to further support the channel flow model (Zhang et al., 2009; Zhao et al., 2012). Impingement of the channel flow against the Yangtze craton would imply simultaneous normal and thrust faulting on both sides of the Longmen Shan (Royden et al., 2008). Yet unlike in the Himalayas, evidence for structures accommodating large-scale normal-sense motion has not been unambiguously reported in the Longmen Shan (Tian et al., 2016). Furthermore, recent seismic studies (e.g., Guo et al., 2013), which image crustal-scale structures and faults, question the channel flow model. Then, consensus on the geodynamics of the eastern Tibet has not been achieved yet. Moreover, in hot orogens such as Tibet, tunneling of weak partially molten, low-viscosity lower to middle crust can generate brittle deformation in the upper crust, especially if it has been deformed prior to the channel flow injection, and the upper and lower crusts remain mechanically coupled (e.g., Beaumont et al., 2001; Medvedev & Beaumont, 2006). Consequently, the two end-member modes of deformation often proposed to debate the evolution of this plateau margin are not mutually exclusive.

Several recent events have contributed to the debate on the eastern Tibetan geodynamics. First, the 2008Mw 7.9 Wenchuan and 2013Mw7.0 Lushan earthquakes demonstrated the seismic potential of the Longmen Shan despite its slow crustal deformation rates (e.g., Burchfiel et al., 2008; Liu-Zeng et al., 2009; Xu et al., 2009). Second, the discovery of the Longriba fault system (LFS), located ~200 km northwest and parallel to the Longmen Shan (Shen et al., 2009), has fostered new questions concerning the accommodation of long wavelength deformation across this part of the plateau (Figure 1a, Ansberque et al., 2015; Guo et al., 2013). The late Quaternary dextral strike-slip activity of the LFS has been demonstrated by paleoseismology and morphotectonic studies (Ansberque et al., 2016; Ren, Xu, Yeats, Zhang, Ding, & Gong, 2013; Ren et al., 2013a; Xu et al., 2008). Geodetic measurements provide evidence that the system partitions deformation at the scale of the entire margin with ~5 mm/yr of right-lateral displacement (Shen et al., 2009). From a morphological point of view, the analysis of denudation rates inferred from cosmogenic radionuclides (CRN) across the LFS emphasizes its role as a major

structural boundary at the millennial timescale preserving the low-relief plateau to the northwest and separating it from the highly dissected margin to the southeast (Figure 1b, Ansberque et al., 2015). These results attest that the LFS is a first-order feature controlling the Quaternary morphological evolution of the eastern Tibetan margin. However, although it has been described as a Triassic inherited structure (de Sigoyer et al., 2014; Guo et al., 2015), clear evidence for its Cenozoic activity supported by quantitative data has not been provided so far. Our study addresses this lack of information by investigating the exhumation history of rocks across the LFS using low-temperature thermochronology. We present new samples collected from each side of the LFS to identify pre-Quaternary activity of the system. Low-temperature thermochronology is a suitable method for investigating million-year timescale thermal histories of exhumed crustal rocks (e.g., Reiners et al., 2005). Furthermore, thermochronology techniques enable quantification of exhumation magnitude, timing, and rates. Our application of thermochronology is focused on identifying if Cenozoic deformation on the LFS was in, or out of, phase with deformation in the Longmen Shan. We conclude with discussion of the relevance of the LFS for proposed deformation models of the eastern Tibetan margin.

## 2. Geological Setting

The LFS is composed of two parallel fault zones, the NW dipping Longriqu fault to the north and the Maoergai fault to the south (Figure 1b; Guo et al., 2013). The LFS is the transition between the Aba block to the northwest and the Longmen Shan block to the southeast (Figure 1a). Both blocks are part of the eastern edge of a large Triassic accretionary wedge, the Songpan Garze terrane, which mostly consists of folded Triassic metasedimentary rocks and is intruded by Triassic granitoid plutons (Figure 1a, e.g., de Sigoyer et al., 2014; Nie et al., 1994). These plutons were emplaced in the Songpan Garze terrane from 239 to 190 Ma and have a large chemical heterogeneity (de Sigoyer et al., 2014) but tend to show a Yangtze craton affinity (e.g., de Sigoyer et al., 2014; Zhang et al., 2006). This affinity suggests that the craton is underthrusting under the eastern Tibetan margin. Guo et al. (2013) and de Sigoyer et al. (2014) proposed that the LFS marks the western limit of this underthrusting, thereby implying a causal link between Yangtze craton underthrust and the LFS in eastern Tibet. This assumption implies an old age (Triassic) of this system. Yet the activity of the LFS has only been only documented so far for the Quaternary, but no data exist for its longer-term (Meso-Cenozoic) activity. Since at least the late Pleistocene, the Longriqu and Maoergai faults are active with a dominant right-lateral component (Ansberque et al., 2016; Ren, Xu, Yeats, Zhang, Ding, & Gong, 2013; Ren et al., 2013a). The Maoergai and Longriqu faults have a Quaternary dextral slip rate of 0.7 to 2.1 mm/yr (from 21 to 9 ka, respectively; Ren, Xu, Yeats, Zhang, Ding, & Gong, 2013) for the first one and ~3.2 mm/yr for the second one (Ansberque et al., 2016). No vertical motion has been documented on the Maoergai fault (Ren, Xu, Yeats, Zhang, Ding, & Gong, 2013), while the Longriqu fault accommodated ~0.1 mm/yr of reverse slip in the Holocene (Figure 1a, Ren et al., 2013a; Xu et al., 2008). Both faults are associated with a clear topographic signature: the hanging wall of the Longriqu fault, to the northwest consisting

of Triassic sedimentary rocks is ~400 m higher than its footwall to the southeast consisting of Quaternary deposits. The Maoergai fault is associated with a large, linear, steep valley cutting into the Yanggon granitoid (Figures 1a and 2). The well-defined traces of the two main faults correspond to Quaternary ruptures, but the distinctive relief associated with both fault zones suggests significant pre-Quaternary activity (Figure 2).

In the Longmen Shan, the Neoproterozoic basement of the Pengguan massif has been exhumed between the Wenchuan and Beichuan faults (Figure 1a). An exhumation magnitude of 20 km associated with slip on the Beichuan fault has been suggested for the range since the Lower Cretaceous (Airaghi et al., 2017). During the Cenozoic, the Longmen Shan experienced two distinct exhumation events at ~30–25 (Wang et al., 2012) and ~10 Ma (Arne et al., 1997; Godard et al., 2009; Kirby et al., 2002; Wang et al., 2012; Figure 1a). In contrast with the Oligocene exhumation phase, the mid-Miocene event is observed across eastern, southeastern, and northeastern Tibet (e.g., Kirby et al., 2002; Lease, 2014; Ouimet et al., 2010; Tian et al., 2015). This mid-Miocene event has also been recorded in the headwater of the Heishui River, southeast of the Maoergai fault (Figures 1b and 2a) at ~10–12 Ma by Tian et al. (2015). The authors suggest a rapid propagation of river incision from the front of the margin (southeast) to the northwest in response to a deformation phase of the Longmen Shan at this period. However, the ultimate headward extent of this incision wave beyond the LFS and whether differential exhumation occurs across the LFS have not been addressed.

### 3. Methods

We used fission track and (U-Th)/He dating on apatites and zircons (apatite (U-Th)/He (AHe), apatite fission track (AFT), zircon (U-Th)/He (ZHe), and zircon fission track (ZFT)), which have closure temperatures ranging from ~60 to ~250°C. These data were used to highlight the Meso-Cenozoic cooling history of the rocks across the LFS. Fission tracks are physical damage to the mineral lattice produced mostly by the spontaneous fission of <sup>238</sup>U, which accumulate and are preserved through time when the host mineral cools below the closure temperature, which is ~80–110°C for apatite (e.g., Gleadow & Lovering, 1978; Wagner, 1968) and 180–250°C for zircon (e.g., Bernet, 2009; Yamada et al., 1995). The (U-Th)/He thermochronometer is based on the in-growth of <sup>4</sup>He produced by the decay of parent isotopes and on its retentivity in its host mineral. In apatite, helium is wholly retained below ~40°C and rapidly diffuses out of the crystal above ~60°C with the intervening temperature interval defining the partial retention zone (e.g., Wolf et al., 1996, 1998). For zircon, the respective closure temperatures are ~130 and 180°C (e.g., Reiners et al., 2002; Wolfe & Stockli, 2010). For both systems, the closure temperature sensitivity depends on the cooling rate, grain size, radiation damage, and effective uranium content (e.g., Ehlers et al., 2005; Shuster et al., 2006). The closure temperature can be converted into a depth estimate after estimating the paleogeothermal gradient; the obtained cooling rate can then be translated into an exhumation rate. On the basis of previous thermochronological

studies conducted on the margin (e.g., Clark, House, et al., 2005; Tian et al., 2015; Wang et al., 2012), we assume a thermal gradient ranging from 20 to 30°C/km constant through time, yielding a record of exhumation from ~3 (AHe) to ~12 km (ZFT). More details on the methodology can be found in the supporting information (Barbarand et al., 2003; Carlson et al., 1999; Farley et al., 1996; Gallagher, 2012; Hurford & Green, 1982; Ketcham et al., 2007).

We measured cooling ages from 13 granitoid samples (Table 1) including two pseudo-vertical profiles located in the  $221 \pm 4$  Ma (emplacement age) Yanggon pluton (Figure 1a; Zhang et al., 2006) on both sides of the Maoergai fault, and additional samples in surrounding areas (Figure 2a). The first profile is located northwest of the Maoergai fault at elevations ranging between 3,520 and 4,223 masl (Mao profile, three samples), which represents the only documented thermochronology vertical profile in this area. The second profile is located ~15 km southeast of the Maoergai fault (Yan profile, six samples) in the Dagu National park, with elevations ranging from 3,851 to 5,000 m asl (Figure 2a). This profile, south of the Maoergai fault, overlaps partly with sampling sites of Tian et al. (2015), which we resampled to ensure consistent data sets from both sides of the Maoergai fault and to avoid apparent age offsets across the fault resulting from different age measurement techniques and laboratory procedures. An additional sample was collected on a small granitoid outcrop located in the hanging wall (northwest) of the Longriqu fault (Figure 2a).

## 4. Results

### 4.1. General Comment on Data Quality

We collected ~4 kg of rocks per samples. Most samples yielded few apatite grains and did not provide a statistically significant number of confined fission track lengths to warrant track length measurement. Samples from the Yan profile were particularly affected by this problem, as samples YanA, Yan3, Yan4, and Yan5 yielded 6, 8, 11, and 6 grains, respectively (Table 2). The Mao profile and Lon sample, which represent key data since they document cooling ages in previously unsampled areas, yielded significantly more material with 20, 20, 11, and 17 grains for Mao1, Mao2, Mao3, and Lon1, respectively (Table 2). The sample mean AFT age encompasses dispersion among single-grain ages and should therefore be averaged over more than 10 grains (Donelick et al., 2005; Tagami & O'Sullivan, 2005). Accordingly, we consider the mean AFT ages obtained along the Mao profile reliable, while we are more cautious with the Yan profile AFT ages. Averaged ZFT ages also suffer from a small number of grains (Table 2), and samples Yan3 and Mao1, Mao2, and Mao3 yielded age data (Table 2). However, despite the small number of zircon grains, all ages passed the  $\chi^2$  test, errors on ZFT ages are typically less than 10%, and mean ZFT ages from the Mao profile correlate with the increase in elevation (Figure 2a and Table 2). We used pooled ages where the probability  $P(\chi^2)$ , representing the age dispersion among the data, is  $>5\%$  and central ages where  $P(\chi^2) < 5\%$  (Table 2; Galbraith, 1981; Galbraith & Laslett, 1993).

The difference of success in obtaining a sufficient number of apatite and zircon grains for the FT method along the Yan and Mao profiles may arise from two issues: (1) spatial heterogeneities in chemical composition within the Yanggon pluton leading to some richer/poorer accessory mineral areas (e.g., Clemens et al., 2010; Morton et al., 1969) or (2) an issue during the heavy mineral separation for the Yan profile samples resulting in a limited quantity of material.

ZHe ages were averaged over two to four single-grain replicates. Although grains of similar size were analyzed, single-grain ages are dispersed, which results in large errors ( $>10$  Ma) in sample mean ZHe ages. Similarly, eU values are strongly dispersed with suspiciously young ages associated with very high-eU grains (Table 3). The latter ages were excluded from mean ZHe age calculation (Guenther et al., 2013) (Table 3). Only one sample yielded an AHe age (Lon1, Table 3); the four dated grains were of poor quality and the possible presence of U-rich micro-inclusions undetected during the grain picking resulted in over-dispersed single-grain ages; therefore, the obtained age should be considered with caution (Table 3). Single-grain (UTh)/He ages are reported with a  $2\sigma$  error based on the reproducibility of standard measurements in the lab. Sample mean ages are reported with a  $1\sigma$  error (Tables 2 and 3). It should be noted that overdispersion among single-apatite or single-zircon FT or (U-Th)/He ages has been reported in several studies as resulting from different grain response either to annealing process in the case of the FT technique (e.g., Tagami & O'Sullivan, 2005) or to spatial variability of U-He concentration and Hediffusivity within the grains for the (U-Th)/He method (Danišik et al., 2017; Farley et al., 2011; Hourigan et al., 2005).

#### 4.2. Fission Track and (U-Th)/He Ages

Southeast of the Maoergai fault, mean AFT ages range between  $6.2 \pm 1.9$  and  $12.9 \pm 1.4$  Ma above 4,000m(asl) (Figure 2a). Most of these ages correlate with elevation except for Yan5 ( $8.0 \pm 1.5$  Ma at 4875 m), which is younger than Yan4 ( $12.9 \pm 1.4$  Ma at 4,748 m; Figure 2a). Yan3 is the only sample from the Yan profile to provide a ZFT age of  $61.4 \pm 4.9$  Ma (4,612 m). Within the Maoergai fault valley and northwest of it, mean AFT ages are older and range from  $19.4 \pm 1.6$  at 3,520 m to  $37.1 \pm 5.2$  Ma at 4,224 m (Figure 2a). Mean ZFT ages along the Mao profile range between  $76.8 \pm 7.6$  at 4,101 m up to  $87.8 \pm 5.6$  Ma at 4,224 m. The correlation between the Mao profile AFT and ZFT ages with elevation (Figure 2a) strengthen our confidence in these ages. Along the Yan profile ZHe mean ages span from  $67.7 \pm 10$  at 4,269m to  $128.4 \pm 40$ Ma at 4,748 m. Northwest of the fault they range from  $91.8 \pm 17.8$  at 4,101 m to  $119.3 \pm 14.7$  Ma at 4,224 m (Figure 2a and Table 3). We note that ZHe ages are older than the ZFT ages (Figure 2a), which is not expected since the closure temperature of the ZHe ( $\sim 180^\circ\text{C}$ ) system should be cooler than that of ZFT ( $\sim 250^\circ\text{C}$ ). This phenomenon, which affects Yan3, Mao2, and Mao3 (Table 1), may be related to the small number of dated zircons for the FT method, although Danišik et al. (2017) emphasize that this age inversion is likely related to some heterogeneities in U-He isotope abundances in zircons and to He trapping by fluid inclusions, which are often observed in



zircons. Tian et al. (2015) reported AFT ages along and aside the Yan profile southeast of the LFS at three similar locations around YanA, Yan4, and Yan5 (Figure 2a zoom-in). From our data set, only Yan5 is significantly different, while AFT ages of YanA and Yan4 are similar to Tian et al. (2015) results, despite the limited number of dated grains.

#### 4.3. Thermal Modeling

To quantitatively evaluate the time-temperature (t-T) history of the sampled rocks, we performed inverse thermal history modeling with HeFTy (Ketcham et al., 2007; Figure 3a) on three individual samples, and we used the QTQt software to jointly model the thermal history of the two vertical profiles (modeling setup is fully provided in Gallagher, 2012) (Figures 3b and 3c). The different modeling approaches allow us to (1) model the t-T history of the single Lon1 sample and to compare it with the southern samples and (2) compare the cooling histories obtained from single sample to the multiple-samples profiles. For both modeling approaches we set the surface conditions at  $0 \pm 10^\circ\text{C}$ , and a starting box at  $220 \pm 10 \text{ Ma}$ – $300 \pm 100^\circ\text{C}$ .

Single-sample thermal modeling was performed on (1) Lon1, which is the westernmost sample of our data set (Figure 3a) for which t-T path has been constrained using its AFT and ZFT ages, (2) Mao2, which provided more AFT grains than Mao3 and Mao1; its t-T path has been constrained using its AFT and ZFT data, and (3) Yan3 which yielded AFT and ZFT ages with reasonably small uncertainties. As most of the plutons in the study area have the same age (de Sigoyer et al., 2014), we decided to set the same conditions for the Longriqu granitoid (Lon1). We expect large uncertainties to arise from these single-sample t-T path models especially in the interval of times between zircon (Cretaceous) and apatite (Late Cenozoic) cooling ages (Figure 3). Vertical profiles t-T modeling was performed on the AFT and ZHe data from the Mao profile samples Mao1, Mao2, and Mao3 and the Yan profile samples Yan1 to Yan6. Because only Yan3 yields a ZFT age, we did not use this system. We used the AFT annealing multikinetik model from Ketcham et al. (2007), and He diffusion kinetic model in apatite and zircon from Gautheron et al. (2009) and Guenthner et al. (2013), respectively, taking into account radiation damage trapping. Modeling multiple samples vertical profiles present the advantage to better constrain the path of rocks through temperature and time; therefore, we expect smaller uncertainties on the QTQt models as compared to the HeFTy ones.

The AFT ages on both sides on the LFS depict two different age trends at similar elevations with older FT ages along the Mao profile (Figure 2a). Accordingly, t-T histories obtained either from single-sample or vertical profiles display two clearly different cooling histories on both sides of the Maoergai fault over the last ~30 Myr (Figure 3). Southeast of the fault, rocks from the Yan profile experienced fast (~6.5°C/Myr) cooling between ~100 and 60 Ma followed by a slight apparent reheating, and a rapid final cooling event at ~7°C/Myr that initiated around ~10–15 Ma (Figure 3c). The apparent reheating

event is not expected since, as far as we know, no volcanism, metamorphism, or significant (>1–2 km thick) sedimentation event has been recorded in this area at this period of time. Tian et al. (2015) have reported shorter mean track length on grains aged ~18–20 Ma (slowly exhumed) than mean track lengths on grains younger than 10 Ma (rapidly exhumed), which do not support a reheating event in this sector. Moreover, the uncertainties on this apparent reheating are large, such that it should be considered with caution. The t-T history of the Yan3 sample is in agreement showing a rapid acceleration in cooling of ~20°C/Myr after ~10 Ma (Figure 3a). We note that the major cooling event depicted by the t-T path of the Yan profile around 10–15 Ma is coherent with the thermal modeling and the 11.5 Ma cooling event obtained by Tian et al. (2015) suggesting that both studies are in agreement for the major mid-Miocene cooling event of the southern side of the LFS.

The rocks of the Mao profile, northwest of the Maoergai fault, experienced a rapid cooling around 100–80 Ma, similar to that derived from the modeling of the Yan profile. This mid-Cretaceous cooling episode is followed by slower cooling and an acceleration in cooling rate at ~25–35 Ma up to 7°C/Myr. In contrast to the Yan profile, the data from the Mao profile indicate neither a reheating event nor rapid mid-Miocene cooling (Figure 3b). The Lon1 and Mao3 samples depict a similar thermal history over the last ~35 Myr with a slow cooling rate ( $\leq 2^\circ\text{C}/\text{Myr}$ ; Figure 3a). It is worth noting that according to the thermal modeling from the vertical profiles, samples on both sides of the Maoergai fault may have resided around 100–250°C for more than 40 Myr (Figure 3), which may have influenced the helium diffusivity and the annealing of radiation damage in the zircons, thereby resulting in an age inversion between the ZFT and ZHe ages for same samples (Danišík et al., 2017).

## 5. Discussion

### 5.1. Mechanisms for Differential Exhumation Across the Maoergai Fault

Our results identify a difference in cooling ages across the Maoergai fault (Figure 3) resulting from different thermal histories that we interpret as spatial variations in rock exhumation across the fault. In particular, we document an AFT age difference of ~15–20 Myr across the Maoergai fault, with Miocene AFT ages (~10–15 Ma) in the southeast contrasting with Eocene-Oligocene ages in the northwest (~25–35 Ma; Figure 5a). Here we discuss the mechanisms that could be responsible for this differential exhumation across the Maoergai fault.

#### 5.1.1. Regressive Erosion and Fluvial Incision

With the exception of sample Yan5, our AFT results from the Yan profile southeast of the Maoergai fault, are consistent with those of Tian et al. (2015) and support their proposition that the 10–12 Ma cooling rate increase is related to the rapid incision of the Heishui River to the northwest responding to the Longmen Shan uplift. Here we analyze if the observed differential exhumation across the Maoergai

fault can still be explained by regressive incision. Both the Yan and Mao profiles are located within the Heishui catchment, but the Mao profile is located farther north upstream of the Yan profile (Figure 4a). If incision along the Heishui River progressed rapidly toward the plateau interior and no differential uplift had occurred across the Maoergai fault, samples from both transects should record coeval cooling and exhumation at similar rates, which is not the case (Figure 3). Kirby et al. (2003) reported the existence of a lithological knickzone along the Heishui River profile corresponding to the Maoergai pluton (Figures 4a and 4b). This knickzone may delay the propagation of the erosion upstream and across the fault during the mid-Miocene and generate a differential amount of incision between the two sampled valleys. In this case, the valleys downstream of the knickzone should yield younger ages at lower elevations than those located upstream of the knickzone. Our data show the contrary: Eocene-Oligocene ages in the Maoergai fault valley are at similar elevations as the mid-Miocene ages in the Heishui valley (Table 1 and Figure 2a). Furthermore, in the case of an erosional wave currently stopped at the location of the Maoergai pluton, one would expect significant differences in the morphology of the two sampled valleys with a relative steepening and deepening of the southern one (Heishui valley), yet the sampled valleys are similar in terms of widths (~5–7 km) and depths (~1 km; Figure 4c). For these reasons, we consider it unlikely that differential exhumation across the Maoergai fault only results from rapid regressive erosion and delayed propagation of river incision up the valley. Instead, it probably reflects tectonic activity on the fault.

#### 5.1.2. Rock Uplift and Faulting

In general, the AFT closure isotherm can be considered as subhorizontal or mimicking the topography prior to fault motion (Ehlers et al., 2001; Glotzbach et al., 2009). For relatively slow exhumation rates (<0.5 mm/yr during 10 Myr) associated with vertical fault motion, a 1-D model of AFT closure temperature shows moderate isotherm vertical advection of a few hundreds of meters (Ehlers et al., 2001) and implies marginal topographic disturbance to AFT ages on the uplifted fault block. The Maoergai fault has been described as a steeply dipping structure (Guo et al., 2013); even though its geometry is not well resolved at the crustal scale, in the absence of other information the rock exhumation path of samples here can be considered vertical, assuming the rock exhumation is primarily driven by dip-slip motion on the fault. In the absence of more thermochronometers data across the range, or information about the fault geometry in this region, a more sophisticated thermal modeling analysis is not warranted.

The AFT age-elevation relationship from the southern Yan profile, together with Tian et al. (2015) data, shows a transition from slow to rapid exhumation at ~10 Ma, whereas no acceleration of exhumation is observed at this period on the northwest Mao profile at similar elevations (Figure 5b). Isochrone surfaces constructed from low-T thermochronology ages can be used as a marker of post-cooling relative vertical displacement across a fault (e.g., Clark et al., 2010). AFT ages northwest of the fault

(Lon1 and Mao samples) suggests that the 20 and 35 Ma isochrone surfaces are horizontal to slightly tilted to the NW (Figure 5a). As no explicit trend can be derived from the southern Yan samples, we construct the 10 Ma isochrone based on the topographic envelope (Figure 5a). An apparent abrupt change in elevations between the ~35 and ~10 Ma isochrones arises across the Maoergai fault (Figure 5a). Lowering the southeastern block by  $1.8 \pm 0.3$  km aligns the two slow exhumation trends obtained from the AFT data (keeping the trend in older ages fixed, Figures 5b and 5c) and reconciles our results north of the fault with that of Tian et al. (2015) into a single exhumation history (Figure 5c). We interpret this ~2 km offset as related to differential rock uplift of the two crustal blocks across the Maoergai fault. Therefore, the exhumation increase at ~10–15 Ma recorded in the Yan profile is mostly due to the Heishui River incision responding to the active uplift of the southeastern block of the Maoergai fault at that time. Differential rock uplift can be generated by different types of fault kinematics. Below, we examine the possibility for strike- or dip-slip faulting to be responsible for the observed signal.

## 5.2. Type of Motion on the LFS

The western tip of the Maoergai fault displays a ~N45 direction (Figure 2) consistent with a restraining bend within the strain field derived from the current regional geodetic displacement vectors (Shen et al., 2009; Figure 2b). Restraining bends induce rock uplift and can generate exhumation and positive topography >1 km (e.g., Cowgill et al., 2004; Duvall et al., 2013), such that the observed differential exhumation across the Maoergai fault could be related to this kinematic setting. However, several observations are not compatible with this possibility: (1) no evidence of localized relief growth is observed along the fault when comparing its western and eastern parts, (2) the Yan profile is not located in a diffuse deformation zone and does not appear bounded by fault splays, and (3) the Yan profile is located ~15 km away from the fault (Figure 4). Also, regarding the geometry of the western tip of the fault (Figures 2b and 4a), if the uplift was related to a restraining bend, it should be more likely located north, not south of it. Additionally, a push up structure could be proposed between the eventual restraining bend and a southern fault inferred from a glacial valley visible on the SRTM image (Figure 2b). Yet once again, the vertical motion accommodated by the push up should be limited in between the structures not beyond. Therefore, we suggest that the observed differential exhumation is probably related to dip-slip motion.

Geophysical data suggest that the Longriqu fault dips to the northwest (Guo et al., 2013), consistent with the geometry of inherited structures in the Longmen Shan (Hubbard & Shaw, 2009). Assuming a similar NW dip for the Maoergai fault implies that the observed differential rock uplift corresponds to a normal (or transtensional) motion on this structure (Figure 5). Faults with a normal sense of motion are common features in the internal part of orogenic wedges (e.g., Graveleau et al., 2012; Platt, 1986), which is in agreement with the position of the LFS in the eastern Tibetan margin (Figure 6a). However, the available seismic images (Guo et al., 2013) do not resolve the geometry of the Maoergai fault; if

this fault dips to the SE the reconstructed exhumation histories would indicate a reverse (or transpressional) motion. In this configuration, the LFS could also be a back thrust to the crustal wedge (e.g., Platt, 1986; Figure 6b). In any case, our results provide the first evidence that the Maoergai fault, and likely the LFS, was active during the mid-Miocene and that the Maoergai fault did accommodate not only a pure strike-slip motion throughout its existence but also a vertical component. Additionally, ages and thermal histories obtained northwest of the Maoergai fault do not display obvious differential exhumation between the Longriku and the Maoergai faults during the late Cenozoic, which suggests that the Longriku fault did not accommodate a large amount of vertical motion—likely <1 km—during this period of time (Figure 5a).

Assuming a 30°C/km geothermal gradient, the Yan profile yields an exhumation rate of  $\sim 0.2 \pm 0.1$  mm/yr in the southern block of the Maoergai fault since the mid-Miocene. This relatively low exhumation rate should not induce significant advection of the AFT closure isotherms and does not impact our first-order observation of a  $\sim 2$  km differential exhumation across the Maoergai fault. This  $\sim 0.2 \pm 0.1$  mm/yr exhumation rate is comparable to Holocene CRN denudation rates obtained south of the fault ( $\sim 0.4$  mm/yr; Ansberque et al., 2015; Figure 1b). The Mao profile yields an exhumation rate of  $\sim 0.1$ – $0.2$  mm/yr according to the Eocene-Oligocene AFT ages and the thermal modeling (Figures 3b and 5b), which is also comparable to the Holocene CRN denudation rates measured north and close of the Maoergai fault which yield slightly slower to similar values ( $<0.2$  mm/yr; Ansberque et al., 2015; Ouimet et al., 2009; Figure 1b). The million-year exhumation and millennial denudation rate patterns therefore appear similar across the fault zone, which would suggest a coupling between the long and short-term denudation on the margin.

Furthermore, the rapid cooling event starting  $\sim 10$ – $15$  Ma inferred from the Yan profile samples is continuous (Figure 3c), such that the differential rock uplift accommodated by the fault might continue into the Quaternary. Paleoseismology studies in the eastern part of the fault show pure strike-slip displacement over the Holocene, and no vertical motion (Ren et al., 2013a; Figure 2), but it is possible that these localized paleoseismological results (Figure 2b) are not representative of deformation along the entire fault. Moreover, using leveling techniques, Hao et al. (2014) measured a modern vertical velocity increase of  $\sim 1.5$  mm/yr across the LFS from west to east, suggesting a modern vertical motion on the system which is consistent with our results. We note that if a change in kinematics had occurred in the LFS from a mid-Miocene dip-slip to a Quaternary strike-slip motion, it would not be captured by the cooling histories presented here because the thermochronology data are insensitive to lateral motion.

**5.3. An Important Structure and a Block Boundary** The Longmen Shan structures, and especially the Beichuan fault (Figure 1a), has accommodated a maximum of 20 km vertical motion since the Lower Cretaceous (Airaghi et al., 2017) with  $\sim 9$ – $10$  km since  $\sim 30$  Ma (based on ZHe data; Wang et al., 2012), which represents almost five times the amount of the vertical displacement we document on the

Maoergai fault. This difference is not surprising since the Beichuan fault accommodates the deformation at the front of the Songpan Garze crust impinging against the Yangtze craton (e.g., Hubbard & Shaw, 2009), while the Maoergai fault is an internal structure of the plateau located ~200 km from the Longmen Shan. Moreover, it seems that the Beichuan fault was reactivated around 10–15 Ma (Wang et al., 2012), which is coeval with the reported activity on the Maoergai fault. Therefore, we propose that the LFS plays an important role in the dynamics of the eastern Tibetan margin since at least 10–15 Ma.

Together with previous thermochronology data on the Longmen Shan (e.g., Wang et al., 2012), we demonstrate that the rapid exhumation of the eastern Tibetan Plateau has been partitioned onto distinct structures over a ~200 km wide zone between the Maoergai fault and Longmen Shan since the mid-Miocene. Ansberque et al. (2015) have proposed a comparable interpretation over the Quaternary period when analysing the CRN denudation rate distribution, suggesting a protracted deformation pattern. The width of this actively denuding and exhuming block is significantly shorter than the >300 km wavelength for a dynamic topographic deflection predicted by some models of channel flow propagation in eastern Tibet (Clark, House, et al., 2005). However, as the rheological behavior of the lower to middle crusts is far from being fully resolved, the abrupt discontinuity observed in the rock exhumation pattern across the Longriba system and the observed 200 km width of deformation band between the LFS and the Longmen Shan front could still be related either to a plastic-translation-like model (Medvedev & Beaumont, 2006) or to a classical brittle deformation in an orogenic wedge context. We consider this 200 km wide band being the rigid SW Longmen Shan block as identified by GPS data and defined by Shen et al. (2009). Hereafter we discuss the evolution of that block with regard to our data set on the LFS and previously published thermochronological data on the eastern Tibetan margin.

A first exhumation phase is observed in our data around ~85–100 Ma, which is recorded both north and south of the Maoergai fault (Figures 3c and 3b). This lower Cretaceous phase has also been documented in the Aba block, which is located northwest of the LFS by Tian et al. (2014) who furthermore demonstrate that this block did not undergo rapid cooling and therefore remained stable since that time. Airaghi et al. (2017) document an earlier exhumation phase at ~120 Ma along the Beichuan fault in the Longmen Shan based on  $^{40}\text{Ar}/^{39}\text{Ar}$  dating on metamorphic white micas crystallized at 280°C, such that this early to late Cretaceous exhumation seems to have progressed from east to west affecting first the Longmen Shan then the SW Longmen Shan and Aba blocks. These observations suggest that the Aba and SW Longmen Shan blocks were coupled in terms of exhumation during the lower Cretaceous. A second exhumation phase that is documented northwest of the Maoergai fault by AFT ages from the Mao profile and Lon1 sample (Figures 3a and 3b), initiated around ~25–35 Ma. Although this event is not well resolved by our data it does coincide with an exhumation phase in the Longmen Shan, where

it is recorded by ZHe ages (Wang et al., 2012) suggesting that this exhumation phase has been faster at the front of the margin than in the hinterland. The possible collective reactivation of the LFS and the Longmen Shan in the Eocene-Oligocene period could mark the onset of the decoupling between the Abo and SW Longmen Shan blocks.

Clear evidence of a (re)activation of the LFS and of activity in the SW Longmen Shan block occurs during the third exhumation phase at 10–15 Ma. As previously mentioned this event coincide with a mid-Miocene event depicted in the Longmen Shan which also continues to present (Wang et al., 2012). In conclusion, the LFS seems to become a major block boundary accommodating some differential motion after the Late Cretaceous and maybe during the Eocene-Oligocene, with a clear reactivation at ~10–15 Ma.

The succession of rapid Cretaceous, slow Eocene-Oligocene, and finally rapid mid-Miocene cooling rates depicted by our low-T thermochronology systems, implies a significant amount of exhumation (or incision) and suggests that the eastern Tibetan margin was characterized by low relief-high elevations before at least the Eocene-Oligocene. Rohrmann et al. (2012), for example, provide a review of low-temperature thermochronology data from the northern, central, and southern Tibet and show that those events are not isolated, but rather regional and likely reflecting the different growth steps of the Plateau. Finally, the mid-Miocene reactivation of the LFS is also coeval with exhumation phases along the nearby sinistral Xianshuihe fault (Chevalier et al., 2017), Kunlun fault (Duvall et al., 2013), which the LFS may have interacted with (Ansberque et al., 2015; Ren et al., 2013b; Figure 1a), and the Haiyuan fault farther north (e.g., Duvall et al., 2013). This raises the question of the distribution of the far-field stresses southeast and northwest of the LFS, and the magnitude of the surrounding vertical-axis block rotations at ~10–15 Ma.

## 6. Conclusion

Here we report cooling histories of rocks located across the LFS from single samples and two vertical profiles from both sides of the southern Maoergai fault. Our results show a contrast of ages and cooling histories across the Maoergai fault. More specifically, northwest of the fault samples record a slow cooling rate since ~25–35 Ma, while southeast of the fault samples experienced a faster cooling rate since ~10–15 Ma. We interpret this cooling contrast as resulting from ~2 km of differential rock uplift accommodated by vertical motion on the Maoergai fault since the mid-Miocene. Previously, activity on the LFS has only been described throughout the Quaternary timescales; we therefore provide the first evidence that the system has been active since at least the mid-Miocene, which is coeval with major thrusting phases on the Longmen Shan frontal structures. The mid-Miocene motion on the LFS together with that of the Longmen Shan may have triggered an increase of fluvial incision, which has been previously proposed, and localized exhumation over a 200 km wide region. Combining existing

thermochronology data from the eastern Tibetan margin suggest that the LFS becomes an important block boundary between the Cretaceous and the mid-Miocene. Our results show the important role of the LFS in the eastern Tibetan Plateau dynamics long before the Quaternary and should be then included in deformation models in the future.

## References

- Airaghi, L., de Sigoyer, J., Lanari, P., Guillot, S., Vidal, O., Monié, P., & Sautter, B. (2017). Total exhumation across the Beichuan fault (Longmen Shan, Sichuan, China) estimated from metamorphic study. *Journal of Asian Earth Sciences*, 140, 108–121. <https://doi.org/10.1016/j.jseas.2017.04.003>
- Ansberque, C., Bellier, O., Godard, V., Lasserre, C., Wang, M., Braucher, R., et al. (2016). The Longriqu fault zone, eastern Tibetan Plateau: Segmentation and Holocene behavior. *Tectonics*, 35(3), 565–585. <https://doi.org/10.1002/2015TC004070>
- Ansberque, C., Godard, V., Bellier, O., de Sigoyer, J., Liu-Zeng, J., Xu, X., et al. (2015). Denudation pattern across the Longriba fault system and implications for a geomorphological evolution of the eastern Tibetan margin. *Geomorphology*, 246, 542–557. <https://doi.org/10.1016/j.geomorph.2015.07.017>
- Arne, D., Worley, B., Wilson, C., Chen, S. F., Foster, D., Luo, Z. L., & Dirks, P. (1997). Differential exhumation in response to episodic thrusting along the eastern margin of the Tibetan plateau. *Tectonophysics*, 280(3-4), 239–256. [https://doi.org/10.1016/S0040-1951\(97\)00040-1](https://doi.org/10.1016/S0040-1951(97)00040-1)
- Barbarand, J., Carter, A., Wood, I., & Hurford, A. (2003). Compositional and structural control of fission-track annealing in apatite. *Chemical Geology*, 198(1-2), 107–137. [https://doi.org/10.1016/S0009-2541\(02\)00424-2](https://doi.org/10.1016/S0009-2541(02)00424-2)
- Beaumont, C., Jamieson, R. A., Nguyen, M. H., & Lee, B. (2001). Mid-crustal channel flow in large hot orogens: Results from coupled thermalmechanical models. In *Slave-Northern Cordillera Lithospheric Evolution (SNORCLE) and Cordilleran Tectonics Workshop* (pp. 112–170). Lithoprobe Secretariat, University of British Columbia Vancouver.
- Bernet, M. (2009). A field-based estimate of the zircon fission-track closure temperature. *Chemical Geology*, 259(3-4), 181–189. <https://doi.org/10.1016/j.chemgeo.2008.10.043>
- Burchfiel, B. C., Chen, Z., Liu, Y., & Royden, L. H. (1995). Tectonics of the Longmen Shan and adjacent regions, central China. *International Geological Review*, 37(8), 661–735. <https://doi.org/10.1080/00206819509465424>
- Burchfiel, B. C., Royden, L. H., van der Hilst, R. D., Hager, B. H., Chen, Z., King, R. W., et al. (2008). A geological and geophysical context for the Wenchuan earthquake of 12 May 2008, Sichuan, People's Republic of China. *GSA Today*, 18(7), 4–11. <https://doi.org/10.1130/GSATG18A.1>
- Carlson, W. D., Donelick, R. A., & Ketcham, R. A. (1999). Variability of apatite fission-track annealing kinetics: I. Experimental results. *American Mineralogist*, 84, 1213–1223.
- Chevalier, M. L., Leloup, P. H., Replumaz, A., Pan, J., Métois, M., & Li, H. (2017). Temporally constant slip rate along the Ganzi fault, NW Xianshuihe fault system, eastern Tibet. *Geological Society of America Bulletin*. <https://doi.org/10.1130/B31691.1>



- Clark, M. K., Bush, J. W. M., & Royden, L. H. (2005). Dynamic topography produced by lower crustal flow against rheological strength heterogeneities bordering the Tibetan Plateau. *Geophysical Journal International*, 162(2), 575–590. <https://doi.org/10.1111/j.1365-246X.2005.02580>
- Clark, M. K., Farley, K. A., Zheng, D., Wang, Z., & Duvall, A. R. (2010). Early Cenozoic faulting of the northern Tibetan Plateau margin from apatite (U–Th)/He ages. *Earth and Planetary Science Letters*, 296(1–2), 78–88. <https://doi.org/10.1016/j.epsl.2010.04.051>
- Clark, M. K., House, M. A., Royden, L. H., Whipple, K. X., Burchfiel, B. C., Zhang, X., & Tang, W. (2005). Late Cenozoic uplift of southeastern Tibet. *Geology*, 33(6), 525–528. <https://doi.org/10.1130/G21265.1>
- Clark, M. K., & Royden, L. H. (2000). Topographic ooze: Building the eastern margin of Tibet by lower crustal flow. *Geology*, 28(8), 703–706. [https://doi.org/10.1130/0091-7613\(2000\)28%3C703:TOBTEM%3E2.0.CO;2](https://doi.org/10.1130/0091-7613(2000)28%3C703:TOBTEM%3E2.0.CO;2)
- Clemens, J. D., Helps, P. A., & Stevens, G. (2010). Chemical structure in granitic magmas—A signal from the source? *Earth and Environmental Science Transactions of the Royal Society of Edinburgh*, 100, 159–172.
- Cowgill, E., Yin, A., Arrowsmith, J. R., Feng, W. X., & Shuanhong, Z. (2004). The Akato Tagh bend along the Altyn Tagh fault, northwest Tibet 1: Smoothing by vertical-axis rotation and the effect of topographic stresses on bend-flanking faults. *Geological Society of America Bulletin*, 116(11–12), 1423–1442. <https://doi.org/10.1130/B25359.1>
- Danišík, M., McInnes, B. I. A., Kirkland, C. L., McDonald, B. J., Evans, N. J., & Becker, T. (2017). Seeing is believing: Visualization of He distribution in zircon and implications for thermal history reconstruction on single crystals. *Science Advances*, 3(2), e1601121. <https://doi.org/10.1126/sciadv.1601121>
- De Michele, M., Raucoules, D., de Sigoyer, J., Pubellier, M., & Chamot-Rooke, N. (2010). Three-dimensional surface displacement of the 2008 May 12 Sichuan earthquake (China) derived from Synthetic Aperture Radar: Evidence for rupture on a blind thrust. *Geophysical Journal International*, 183, 1097–1103. <https://doi.org/10.1111/j.1365-246X.2010.04807.x>
- De Sigoyer, J., Vanderhaeghe, O., Duchêne, S., & Billerot, A. (2014). Generation and emplacement of Triassic granitoids within the Songpan Ganze accretionary-orogenic wedge in a context of slab retreat accommodated by tear faulting, Eastern Tibetan plateau, China. *Journal of Asian Earth Sciences*, 88, 192–216. <https://doi.org/10.1016/j.jseaes.2014.01.010>
- Densmore, A., Ellis, M. A., Li, Y., Zhou, R., Hancock, G. S., & Richardson, N. (2007). Active tectonics of the Beichuan and Pengguan faults at the eastern margin of the Tibetan Plateau. *Tectonics*, 26, TC4005. <https://doi.org/10.1029/2006TC001987>
- Donelick, R. A., O’Sullivan, P. B., & Ketcham, R. A. (2005). Apatite fission-track analysis. *Reviews in Mineralogy and Geochemistry*, 58(1), 49–94. <https://doi.org/10.2138/rmg.2005.58.3>
- Duvall, A., Clark, M., Kirby, E., Farley, K. A., Craddock, W. H., Li, C., & Yuan, D. (2013). Low-temperature thermochronometry along the Kunlun and Haiyuan Faults, NE Tibetan Plateau: Evidence for kinematic change during late-stage orogenesis. *Tectonics*, 32, 1190–1211. <https://doi.org/10.1002/tect.20072>
- Ehlers, T. A., Armstrong, P. A., & Chapman, D. S. (2001). Normal fault thermal regimes and the interpretation of low-temperature thermochronometers. *Physics of the Earth and Planetary Interiors*, 126(3–4), 179–194. [https://doi.org/10.1016/S0031-9201\(01\)00254-0](https://doi.org/10.1016/S0031-9201(01)00254-0)

Ehlers, T. A., Chaudhri, T., Kumar, S., Fuller, C. W., Willett, S. D., Ketcham, R. A., et al. (2005). Computational tools for low-temperature thermochronometers interpretation. *Reviews in Mineralogy and Geochemistry*, 58(1), 589–622. <https://doi.org/10.2138/rmg.2005.58.22>

Farley, K. A., Wolf, R. A., & Silver, L. T. (1996). The effects of long alpha-stopping distances on U-Th/He dates. *Geochimica et Cosmochimica Acta*, 60(21), 4223–4229. [https://doi.org/10.1016/S0016-7037\(96\)00193-7](https://doi.org/10.1016/S0016-7037(96)00193-7)

Farley, K. A., Shuster, D. L., & Ketcham, R. A. (2011). U and Th zonation in apatite observed by laser ablation ICPMS, and implications for the (U–Th)/He system. *Geochimica et Cosmochimica Acta*, 75(16), 4515–4530. <https://doi.org/10.1016/j.gca.2011.05.020>

Feng, S-y., Zhang, P-z., Liu, B-j., Wang, M., Zhu, S-b., Ran, Y-k., et al. (2016). Deep curstal deformation of the Longmen Shan, eastern Tibetan Plateau, from seismic reflection and Finite Element modeling. *Journal of Geophysical Research: Solid Earth*, 121, 767–787. <https://doi.org/10.1002:2015JB012352>

Galbraith, R. F. (1981). On statistical models for fission track counts. *Mathematical Geology*, 13(6), 471–478. <https://doi.org/10.1007/BF01034498>

Galbraith, R. F., & Laslett, G. M. (1993). Statistical models for mixed fission track ages. *Nuclear Tracks and Radiation Measurements*, 21(4), 459–470. [https://doi.org/10.1016/1359-0189\(93\)90185-C](https://doi.org/10.1016/1359-0189(93)90185-C)

Gallagher, K. (2012). Transdimensional inverse thermal history modeling for quantitative thermochronology. *Journal of Geophysical Research*, 117, B02408. <https://doi.org/10.1029/2011JB008825>

Gautheron, C., Tassan-Got, L., Barbarand, J., & Pagel, M. (2009). Effect of alpha-damage annealing on apatite (U–Th)/He thermochronology. *Chemical Geology*, 266(3–4), 157–170. <https://doi.org/10.1016/j.chemgeo.2009.06.001>

Gleadows, A. J. W., & Lovering, J. F. (1978). Thermal history of granitic rocks from western Victoria: A fission-track dating study. *Journal of the Geological Society of Australia*, 25(5-6), 323–340. <https://doi.org/10.1080/00167617808729039>

Glottzbach, C., Spiegel, C., Reinecker, J., Rahn, M., & Frisch, W. (2009). What perturbs isotherms? An assessment using fission-track thermochronology and thermal modelling along the Gotthard transect, Central Alps. In F. Lisker, B. Ventura, & U. A. Glasmacher (Eds.), *Thermochronological methods: From palaeotemperature constraints to landscape evolution models*, Geological Society, London, Special Publications (Vol. 324, pp. 111–124). <https://doi.org/10.1144/SP324.9>

Godard, V., Pik, R., Lavé, J., Cattin, R., Tibari, B., de Sigoyer, J., & Pubellier, M. (2009). Late Cenozoic evolution of the central Longmen Shan, eastern Tibet: Insight from (U–Th)/He thermochronometry. *Tectonics*, 28, TC5009. <https://doi.org/10.1029/2008TC002407>

Godard, V., Lavé, J., Carcaillet, J., Cattin, R., Bourlès, D., & Zhu, J. (2010). Spatial distribution of denudation in Eastern Tibet and regressive erosion of plateau margins. *Tectonophysics*, 491(1-4), 253–274. <https://doi.org/10.1016/j.tecto.2009.10.026>

Graveleau, F., Malavieille, J., & Dominguez, S. (2012). Experimental modelling of orogenic wedges: A review. *Tectonophysics*, 538-540, 1–66. <https://doi.org/10.1016/j.tecto.2012.01.027>

Guenther, W. R., Reiners, P. W., Ketcham, R. A., Nasdala, L., & Giester, G. (2013). Helium diffusion in natural zircon: Radiation damage, anisotropy, and the interpretation of zircon (U–Th)/He

thermochronology. *American Journal of Science*, 313(3), 145–198.  
<https://doi.org/10.2475/03.2013.01>

Guo, X., Gao, R., Keller, G. R., Xu, X., Wang, H., & Li, W. (2013). Imaging the crustal structure beneath the eastern Tibetan Plateau and implications for the uplift of the Longmen Shan range. *Earth and Planetary Science Letters*, 379, 72–80. <https://doi.org/10.1016/j.epsl.2013.08.005>

Guo, X., Gao, R., Xu, X., Keller, G. R., Yin, A., & Xiong, X. (2015). Longriba fault zone in eastern Tibet: An important tectonic boundary marking the westernmost edge of the Yangtze block. *Tectonics*, 34, 970–985. <https://doi.org/10.1002/2015TC003880>

Hao, M., Wang, Q., Shen, Z., Cui, D., Ji, L., Li, Y., & Qin, S. (2014). Present day crustal vertical movement inferred from precise leveling data in eastern margin of Tibetan Plateau. *Tectonophysics*, 632, 281–292. <https://doi.org/10.1016/j.tecto.2014.06.016>

Hourigan, J. K., Reiners, P. W., & Brandond, M. (2005). U-Th zonation-dependent alpha-ejection in (U-Th)/He chronometry. *Geochimica et Cosmochimica Acta*, 69(13), 3349–3365.  
<https://doi.org/10.1016/j.gca.2005.01.024>

Hubbard, J., & Shaw, J. H. (2009). Uplift of the Longmen Shan and Tibetan Plateau, and the 2008 Wenchuan (M = 7.9) earthquake. *Nature*, 458(7235), 194–197. <https://doi.org/10.1038/nature07837>

Hurford, A. J., & Green, P. F. (1982). A users' guide to fission track dating calibration. *Earth and Planetary Science Letters*, 59(2), 343–354. [https://doi.org/10.1016/0012-821X\(82\)90136-4](https://doi.org/10.1016/0012-821X(82)90136-4)

Ketcham, R. A., Carter, A., Donelick, R. A., Barbarand, J., & Hurford, A. J. (2007). Improved measurement of fission-track annealing in apatite using c-axis projection. *American Mineralogist*, 92(5-6), 789–798. <https://doi.org/10.2138/am.2007.2280>

Kirby, E., Reiners, P. W., Krol, M. A., Whipple, K. X., Hodges, K. V., Farley, K. A., & Chen, Z. (2002). Late Cenozoic evolution of the eastern margin of the Tibetan Plateau : Inferences from <sup>40</sup>Ar/<sup>39</sup>Ar and (U–Th)/He thermochronology. *Tectonics*, 21, 1001. <https://doi.org/10.1029/2000TC001246>

Kirby, E., Whipple, K. X., Burchfiel, B. C., Tang, W., Berger, G., Sun, Z., & Chen, Z. (2000). Neotectonics of the Min Shan, China: Implications for mechanisms driving Quaternary deformation along the eastern margin of the Tibetan Plateau. *Geological Society of America Bulletin*, 112(3), 375–393. [https://doi.org/10.1130/0016-7606\(2000\)112%3C375:NOTMSC%3E2.0.CO;2](https://doi.org/10.1130/0016-7606(2000)112%3C375:NOTMSC%3E2.0.CO;2)

Kirby, E. K. X., Whipple, W. T., & Chen, Z. (2003). Distribution of active rock uplift along the eastern margin of the Tibetan Plateau: Inferences from bedrock channel longitudinal profiles. *Journal of Geophysical Research*, 108(B4), 2217. <https://doi.org/10.1029/2001JB000861>

Lease, R. O. (2014). Cenozoic mountain building on the northeastern Tibetan Plateau. *Geological Society of America Special Papers*, 507, 115–127.  
[https://doi.org/10.1130/2014.2507\(06\)%E2%80%8B](https://doi.org/10.1130/2014.2507(06)%E2%80%8B)

Liu-Zeng, J., Zhang, Z., Wen, L., Tapponnier, P., Sun, J., Xing, X., & van der Woerd, J. (2009). Coseismic ruptures of the 12 May 2008, Ms 8.0 Wenchuan earthquake, Sichuan: East–west crustal shortening on oblique, parallel thrusts along the eastern edge of Tibet. *Earth and Planetary Science Letters*, 286(3-4), 355–370. <https://doi.org/10.1016/j.epsl.2009.07.017>

Liu-Zeng, J., Wen, L., Oskin, M., & Zeng, L. (2011). Focused modern denudation of the Longmen Shan margin. *Geochemistry, Geophysics, Geosystems*, 12, Q11007.  
<https://doi.org/10.1029/2011GC003652>

Medvedev, A., & Beaumont, C. (2006). Growth of continental plateaus by channel injection: Models designed to address constraints and thermomechanical consistency. In R. D. Law, M. P. Searle, & L. Godin (Eds.), *Channel flow, ductile extrusion and exhumation in continental collision zones*, Geological Society, London, Special Publications (Vol. 268, pp. 147–164).

Morton, D. M., Braid, A. K., & Braid, K. W. (1969). The Lakeview Mountains pluton, southern California batholith: Part II. Chemical composition and variation. *Geological Society of America Bulletin*, 80(8), 1553–1564. [https://doi.org/10.1130/0016-7606\(1969\)80%5B1553:TLMPSC%5D2.0.CO;2](https://doi.org/10.1130/0016-7606(1969)80%5B1553:TLMPSC%5D2.0.CO;2)

Nie, S., Yin, A., Rowley, D. B., & Yin, Y. (1994). Exhumation of the Dabie Shan ultra-high pressure rocks and accumulation of the Songpan Ganzi flysch sequence, central China. *Geology*, 22(11), 999–1002. [https://doi.org/10.1130/0091-7613\(1994\)022%3C0999:EOTDSU%3E2.3.CO;2](https://doi.org/10.1130/0091-7613(1994)022%3C0999:EOTDSU%3E2.3.CO;2)

Ouimet, W., Whipple, K., Royden, L., Reiners, P., Hodges, K., & Pringle, M. (2010). Regional incision in eastern margin of the Tibetan Plateau. *Lithosphere*, 2(1), 50–63. <https://doi.org/10.1130/L57.1>

Ouimet, W. B., Whipple, K. X., & Granger, D. E. (2009). Beyond threshold hillslopes: Channel adjustment to base-level fall in tectonically active mountain ranges. *Geology*, 37(7), 579–582. <https://doi.org/10.1130/G30013A.1>

Parker, R. N., Densmore, A. L., Rosser, N. J., De Michele, M., Li, Y., Huang, R., et al. (2011). Mass wasting triggered by the 2008 Wenchuan earthquake is greater than orogenic growth. *Nature Geoscience*, 4(7), 449–452.

Platt, J. P. (1986). Dynamics of orogenic wedges and the uplift of high-pressure metamorphic rocks. *Geological Society of America Bulletin*, 97(9), 1037–1053. [https://doi.org/10.1130/0016-7606\(1986\)97%3C1037:DOOWAT%3E2.0.CO;2](https://doi.org/10.1130/0016-7606(1986)97%3C1037:DOOWAT%3E2.0.CO;2)

Qi, W., Xuejun, Q., Qigui, L., Freymueller, J., Shaomin, Y., Caijun, X., et al. (2011). Rupture of deep faults in the 2008 Wenchuan earthquake and uplift of the Longmen Shan. *Nature Geoscience*, 4(9), 634.

Reiners, P. W., Ehlers, T. A., & Zeitler, P. K. (2005). Past, present and future of thermochronology. *Reviews in Mineralogy and Geochemistry*, 58(1), 1–18. <https://doi.org/10.2138/rmg.2005.58.1>

Reiners, P. W., Farley, K. A., & Hickes, H. J. (2002). He diffusion and (U-Th)/He thermochronometry of zircon: Initial results from Fish Canyon Tuff and Gold Butte, Nevada. *Tectonophysics*, 349(1–4), 297–308. [https://doi.org/10.1016/S0040-1951\(02\)00058-6](https://doi.org/10.1016/S0040-1951(02)00058-6)

Ren, J., Xu, X., Yeats, R. S., & Zhang, S. (2013a). Latest Quaternary paleoseismology and slip rates of the Longriba fault zone, eastern Tibet: Implications for fault behavior and strain partitioning. *Tectonics*, 32(2), 216–238. <https://doi.org/10.1002/tect.20029>

Ren, J., Xu, X., Yeats, R. S., & Zhang, S. (2013b). Millennial slip rates of the Tazang fault, the eastern termination of Kunlun fault: Implications for strain partitioning in eastern Tibet. *Tectonophysics*, 608, 1180–1200. <https://doi.org/10.1016/j.tecto.2013.06.026>

Ren, J., Xu, X., Yeats, R. S., Zhang, S., Ding, R., & Gong, Z. (2013). Holocene paleoearthquakes of the Maoergai fault, eastern Tibet. *Tectonophysics*, 590, 121–135. <https://doi.org/10.1016/j.tecto.2013.01.017>

Richardson, N. J., Densmore, A. L., Seward, D., Fowler, A., Wipf, M., Ellis, M. A., et al. (2008). Extraordinary denudation in the Sichuan Basin: Insights from low-temperature thermochronology adjacent to the eastern margin of the Tibetan Plateau. *Journal of Geophysical Research*,

113, B04409. <https://doi.org/10.1029/2006JB004739>

Robert, A., Zhu, J., Vergne, J., Cattin, R., Chan, L. S., Wittlinger, G., et al. (2009). Crustal structures in the area of the 2008 Sichuan earthquake from seismologic and gravimetric data. *Tectonophysics*, 491(1-4), 205–210. <https://doi.org/10.1016/j.tecto.2009.11.010>

Rohrmann, A., Kapp, P., Carrapa, B., Reiners, P. W., Guynn, J., Ding, L., & Heizler, M. (2012). Thermochronologic evidence for plateau formation in central Tibet by 45 Ma. *Geology*, 40(2), 187–190. <https://doi.org/10.1130/G32530>

Royden, L., Burchfiel, B., King, R., Wang, E., Chen, Z., Shen, F., & Liu, Y. (1997). Surface deformation and lower crustal flow in Eastern Tibet. *Science*, 276(5313), 788–790. <https://doi.org/10.1126/science.276.5313.788>

Royden, L. H., Burchfiel, B. C., & van der Hilst, R. D. (2008). The geological evolution of the Tibetan Plateau. *Science*, 321(5892), 1054–1058. <https://doi.org/10.1126/science.1155371>

Shen, Z. K., Sun, J., Zhang, P., Wan, Y., Wang, M., Bürgmann, R., et al. (2009). Slip maxima at fault junctions and rupturing of barriers during the 2008 Wenchuan earthquake. *Nature Geoscience*, 2(10), 718–724. <https://doi.org/10.1038/ngeo636>

Shuster, D. L., Flowers, R. M., & Farley, K. A. (2006). The influence of natural radiation damage on helium diffusion kinetics in apatite. *Earth and Planetary Science Letters*, 249(3-4), 148–161. <https://doi.org/10.1016/j.epsl.2006.07.028>

Tagami, T., & O’Sullivan, P. B. (2005). Fundamentals of fission-track thermochronology. *Reviews in Mineralogy and Geochemistry*, 58(1), 19–47. <https://doi.org/10.2138/rmg.2005.58.2>

Tapponnier, P., Xu, Z., Roger, F., Meyer, B., Arnaud, N., Wittlinger, G., & Yang, J. (2001). Oblique stepwise rise and growth of the Tibet Plateau. *Science*, 294(5547), 1671–1677. <https://doi.org/10.1126/science.105978>

Thiede, R. C., & Ehlers, T. A. (2013). Large spatial and temporal variations in Himalayan denudation. *Earth and Planetary Science Letters*, 371-372, 278–293. <https://doi.org/10.1016/j.epsl.2013.03.004>

Tian, Y., Kohn, B. P., Gleadow, A. J. W., & Hu, S. (2013). Constructing the Longmen Shan eastern Tibetan Plateau margin: Insights from low-temperature thermochronology. *Tectonics*, 32, 576–592. <https://doi.org/10.1002/tect.20043>

Tian, Y., Kohn, B. P., Hu, S., & Gleadow, A. J. W. (2014). Postorogenic rigid behavior of the eastern Songpan-Ganze terrane: Insights from low-temperature thermochronology and implications for intracontinental deformation in central Asia. *Geochemistry, Geophysics, Geosystems*, 15, 453–474. <https://doi.org/10.1002/2013GC004951>

Tian, Y., Kohn, B. P., Hu, S., & Gleadow, A. J. W. (2015). Synchronous fluvial response to surface uplift in the eastern Tibetan Plateau: Implications for crustal dynamics. *Geophysical Research Letters*, 42, 29–35. <https://doi.org/10.1002/2014GL062383>

Tian, Y., Kohn, B. P., Phillips, D., Hu, S., Gleadow, A. J. W., & Carter, A. (2016). Late Cretaceous-earliest Paleogene deformation in the Longmen Shan fold-and-thrust belt, eastern Tibetan Plateau margin: Pre-Cenozoic thickened crust? *Tectonics*, 35, 2293–2312. <https://doi.org/10.1002/2016TC004182>

Vanderhaeghe, O., Medvedev, S., Fullsack, P., Beaumont, C., & Jamieson, R. A. (2003). Evolution of orogenic wedges and continental plateaux: insights from crustal thermal-mechanical models overlying



subducting mantle lithosphere. *Geophysical Journal International*, 153(1), 27–51.  
<https://doi.org/10.1046/j.1365-246X.2003.01861.x>

Wagner, R. (1968). Fission track dating of apatites. *Earth and Planetary Science Letters*, 4(5), 411–415. [https://doi.org/10.1016/0012-821X\(68\)90072-1](https://doi.org/10.1016/0012-821X(68)90072-1)

Wang, E., Kirby, E., Furlong, K. P., van Soest, M., Xu, G., Shi, X., et al. (2012). Two-phase growth of high topography in eastern Tibet during the Cenozoic. *Nature Geoscience*, 5(9), 640–645.  
<https://doi.org/10.1038/ngeo1538>

Wang, W., Godard, V., Liu-Zeng, J., Sherler, D., Xu, C., Zhang, J., et al. (2017). Perturbation of fluvial sediment fluxes following the 2008 Wenchuan earthquake. *Earth Surface Processes and Landforms*. <https://doi.org/10.1002/esp.4210>

Wilson, C. J. L., & Fowler, A. P. (2011). Denudational response to surface uplift in east Tibet: Evidence from apatite fission-track thermochronology. *Geological Society of America Bulletin*, 123(9-10), 1966–1987. <https://doi.org/10.1130/B30331.1>

Wolf, R. A., Farley, K. A., & Kass, D. M. (1998). Modeling of the temperature sensitivity of the apatite (U-Th)/He thermochronometer. *Chemical Geology*, 148, 105–114.

Wolf, R. A., Farley, K. A., & Silver, L. T. (1996). Helium diffusion and low-temperature thermochronometry of apatite. *Geochimica et Cosmochimica Acta*, 60(21), 4231–4240.  
[https://doi.org/10.1016/S0016-7037\(96\)00192-5](https://doi.org/10.1016/S0016-7037(96)00192-5)

Wolfe, M. R., & Stockli, D. F. (2010). Zircon (U-Th)/He thermochronometry in the KTB drill hole, Germany, and its implications for bulk He diffusion kinetics in zircon. *Earth and Planetary Science Letters*, 295(1-2), 69–82. <https://doi.org/10.1016/j.epsl.2010.03.025>

Xu, X., Wen, X., Chen, G., & Yu, G. (2008). Discovery of the Longriba fault zone in eastern Bayan Har block, China and its tectonic implication. *Science in China Series D: Earth Sciences*, 51(9), 1209–1223. <https://doi.org/10.1007/s11430-008-0097-1>

Xu, X., Wen, X., Yu, G., Chen, G., Klinger, Y., Hubbard, J., & Shaw, J. (2009). Coseismic reverse- and oblique-slip surface faulting generated by the 2008 Mw 7.9 Wenchuan earthquake, China. *Geology*, 37(6), 515–518. <https://doi.org/10.1130/G25462A.1>

Yamada, R., Tagami, T., & Nishimura, S. (1995). Confined fission-track length measurement of zircon: Assessment of factors affecting the paleotemperature estimate. *Chemical Geology*, 119(1-4), 293–306. [https://doi.org/10.1016/0009-2541\(94\)00108-K](https://doi.org/10.1016/0009-2541(94)00108-K)

Yan, D.-P., Zhou, M.-F., Li, S.-B., & Wei, G.-Q. (2011). Structural and geochronological constraints on the Mesozoic-Cenozoic tectonic evolution of the Longmen Shan thrust belt, eastern Tibetan Plateau. *Tectonics*, 30, TC6005. <https://doi.org/10.1029/2011TC002867>

Zhang, H. F., Zhang, L., Harris, N., Jin, L.-L., & Yuan, H. (2006). U–Pb zircon ages, geochemical and isotopic compositions of granitoids in Songpan-Garze fold belt, eastern Tibetan Plateau: Constraints on petrogenesis and tectonic evolution of the basement. *Contributions to Mineralogy and Petrology*, 152(1), 75–88. <https://doi.org/10.1007/s00410-006-0095-2>

Zhang, Z., Wang, Y., Chen, Y., Houseman, G. A., Tian, X., Wang, E., & Teng, J. (2009). Crustal structure across Longmenshan fault belt from passive source seismic profiling. *Geophysical Research Letters*, 36, L17310. <https://doi.org/10.1029/2009GL039580>

Zhao, G., Unsworth, M. J., Zhan, Y., Wang, L., Chen, X., Jones, A. G., et al. (2012). Crustal structure and rheology of the Longmenshan and Wenchuan Mw 7.9 earthquake epicentral area from magnetotelluric data. *Geology*, 40(12), 1139–1142. <https://doi.org/10.1130/G33703.1>

#### Caption

Figure 1. (a) Structural map of the eastern Tibetan Plateau. B.F = Beichuan fault, P.F = Pengguan fault, W.F = Wenchuan fault. (b) Topographic profile along a 60 km large swath profile (AA0). Cosmogenic radionuclide (CRN) denudation rates (Ansberque et al., 2015; Godard et al., 2010; Ouimet et al., 2009) and apatite fission track (AFT) ages (Arne et al., 1997; Richardson et al., 2008; Tian et al., 2014, 2015; Wang et al., 2012; Wilson & Fowler, 2011; Yan et al., 2011; this study). LFS = Longriba fault system.

Figure 2. (a) (left) Location map of the thermochronology data collected across the Maoergai fault. The fault mapping is made from Pleiades images. Zoom-in shows the location of Tian et al.'s (2015) data. (b) Shaded digital elevation model of the Maoergai fault valley. Pink dots localize the paleoseismology sites of Ren, Xu, Yeats, Zhang, Ding and Gong (2013). SRTM = Shuttle Radar Topography Mission.

Figure 3. (a) Thermal history modeling of sample Lon1, Mao2, and Yan3 (HeFTy software). Large uncertainty (grey arrow) correspond to unresolved t-T paths due to long interval of time between zircon and apatite ages. Red horizontal arrow depicts the principal cooling event. (b) and (c) T-t paths of the two vertical profiles (QTQt software).

Figure 4. (a) Location map of the topographic profiles. (b) Along-channel profile of the Heishui River localizing the Maoergai pluton and related knickzone. (c) Topographic profiles of the sampled valleys. (d) Swath profile across the Maoergai fault zone.

Figure 5. (a) Schematic isochrones profile inferred from apatite fission tracks (AFT) obtained ages. Topographic profile is a 20 km wide swath profile zoom into the study area (AA', Figure 1). (b) Age-elevation relationship of the AFT data from the two vertical profiles. (c) Composite plot of the AFT ages with a ~2 km shift southeast of the Maoergai fault. The blue trend serves of reference and is fixed.

Figure 6. Bloc diagrams of the Longriba fault system (LFS) in the eastern Tibetan margin setting (adapted from Guo et al., 2013). (a) Structural context with the Maoergai fault accommodating a normal faulting with a NW dip. In this context a negative flower structure is envisaged, formed by the Maoergai and Longriqu faults shaping a basin in which modern deposits are accumulated. (b) Both faults are SE dipping representing hinterland back thrusts of a frontal orogenic wedge in the Longmen Shan. LMS = Longmen Shan.

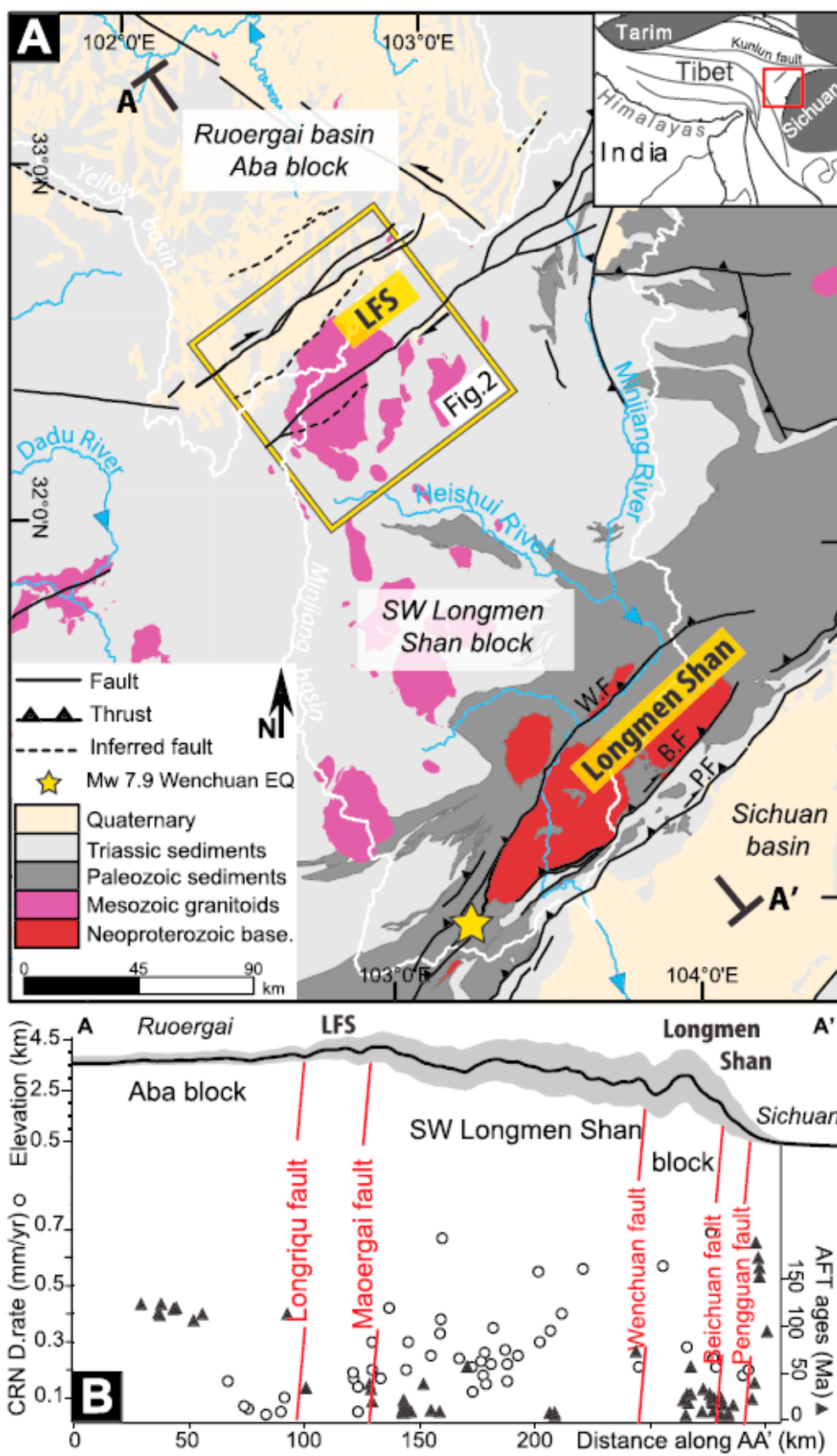


Figure 1



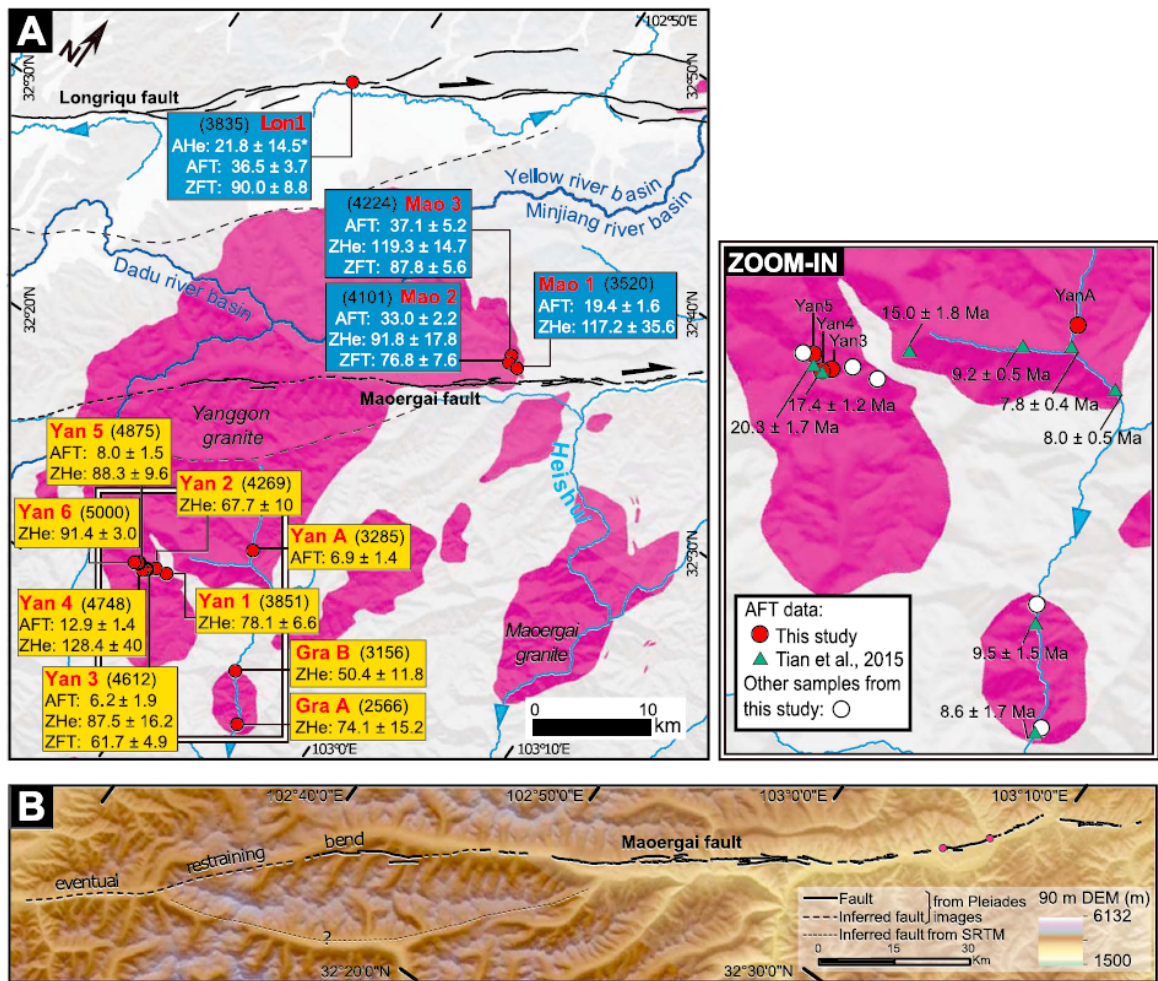


Figure 2

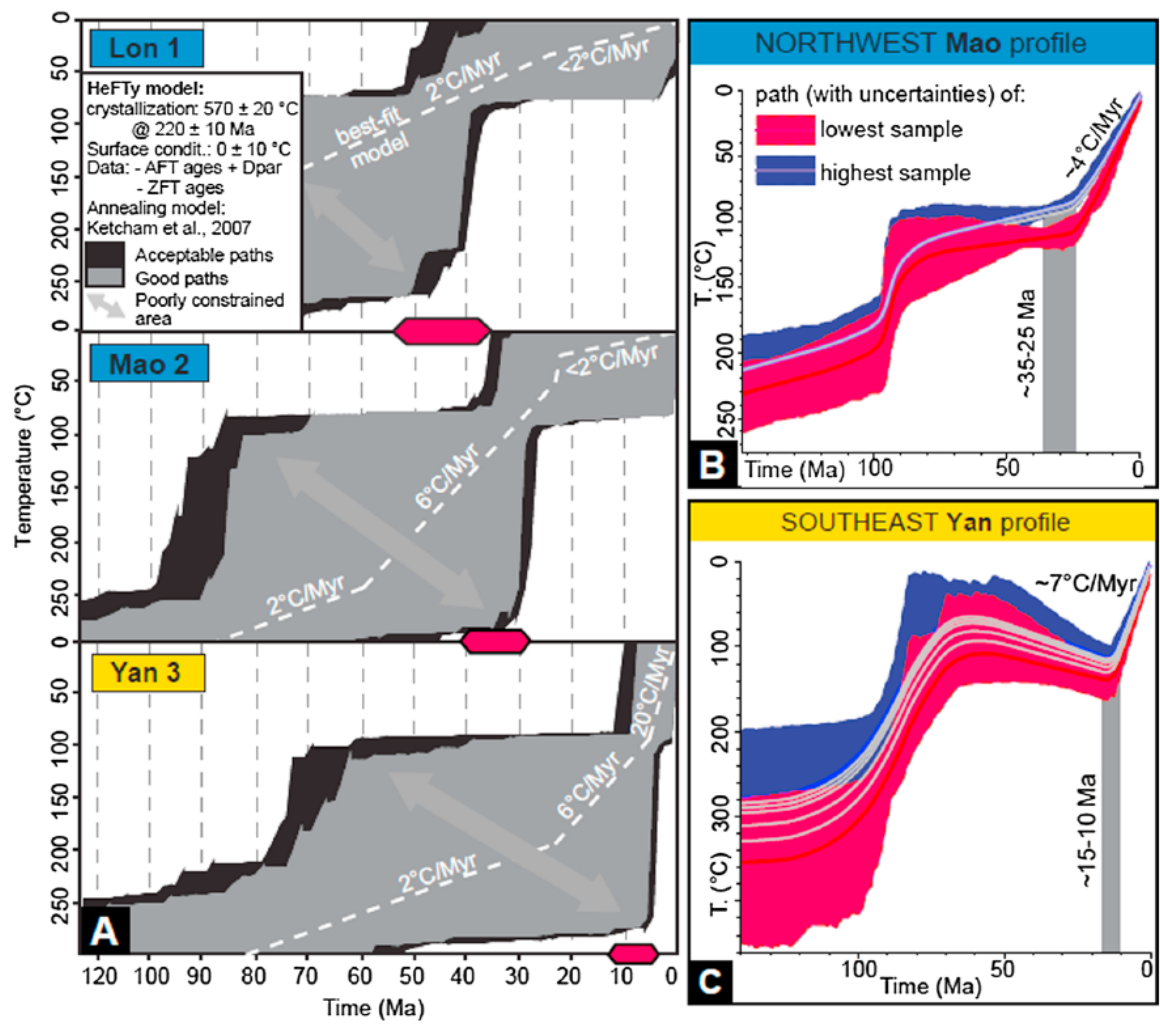


Figure 3

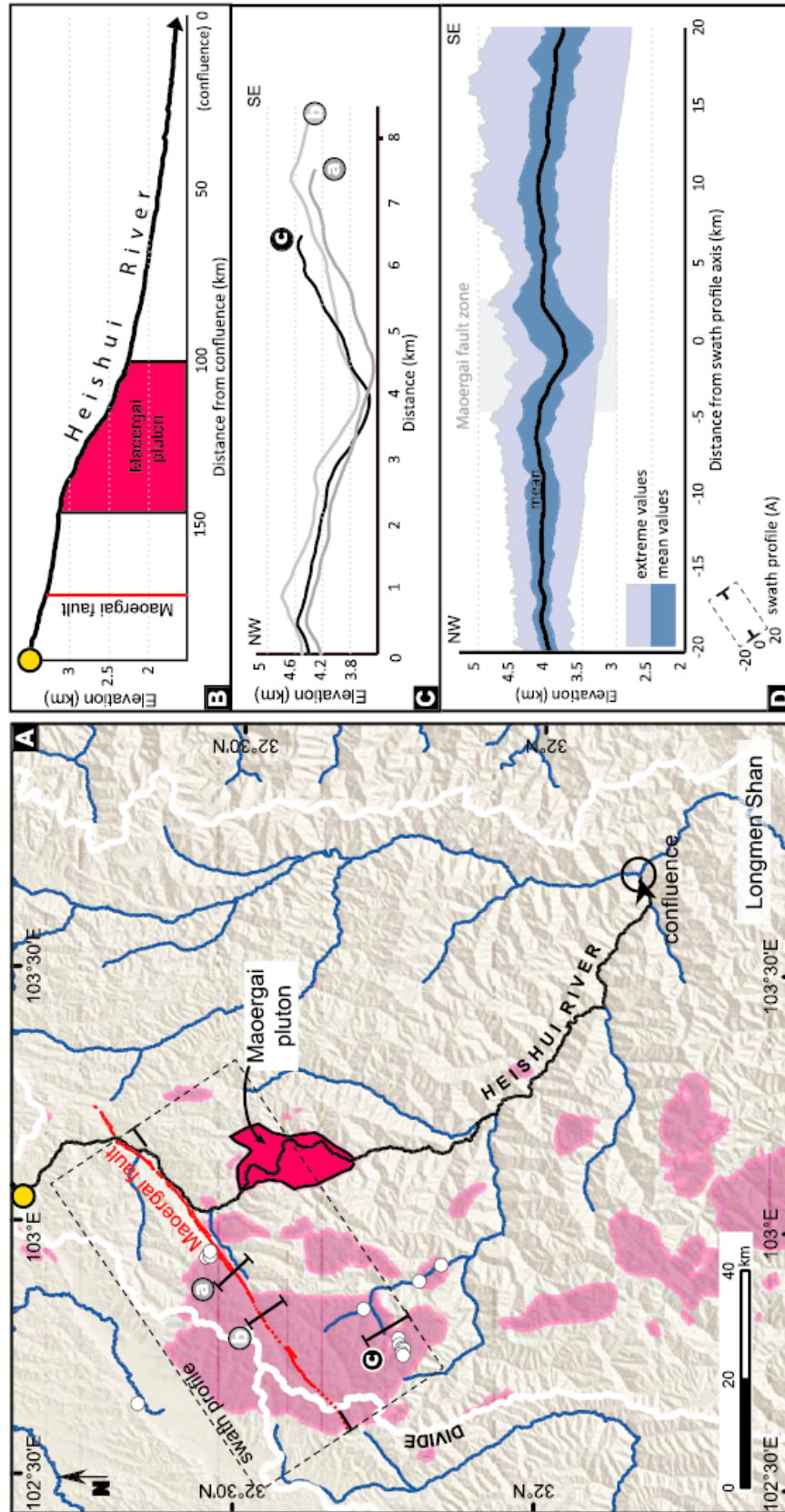


Figure 4

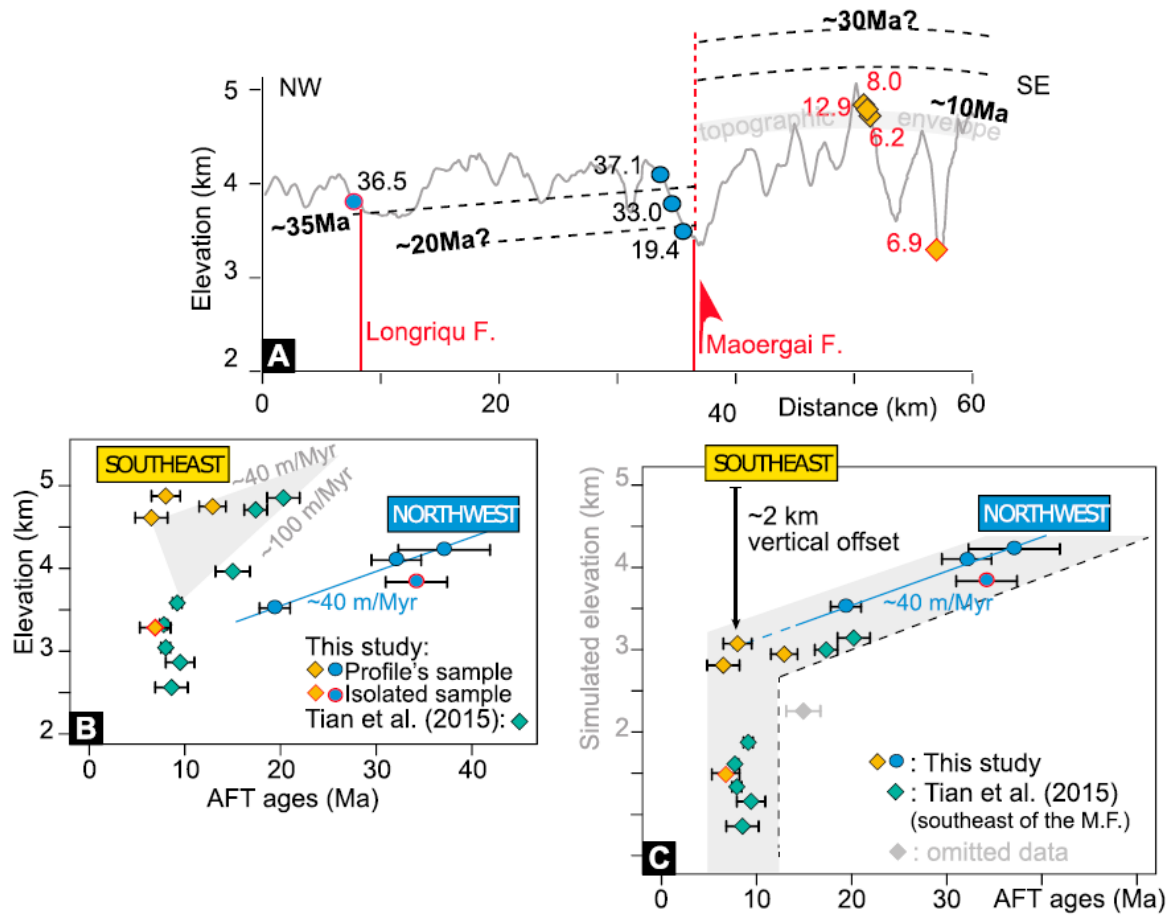


Figure 5

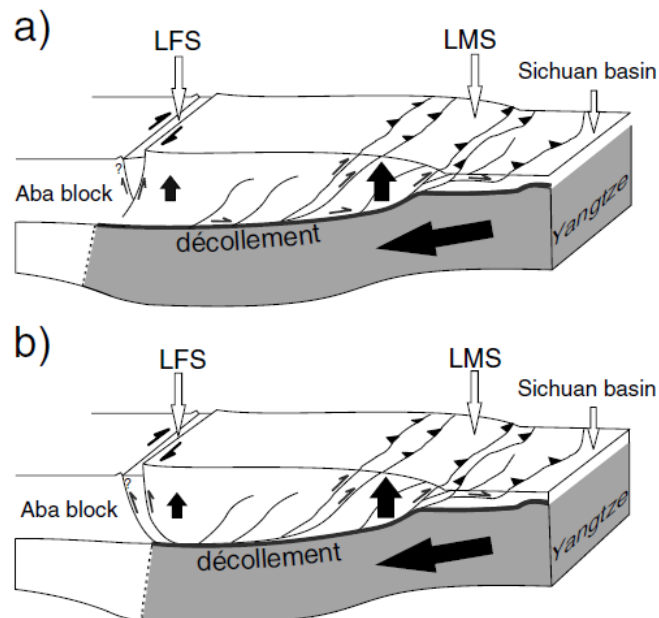


Figure 6



**Table 1**  
*Samples*

Sample	Granitoid name	Longitude (°E)	Latitude (°N)	Elevation (m)	Dating method
YanA	Yanggon	102.838	32.290	3285	AFT
<b>Yan1</b>	Yanggon	102.782	32.231	3851	ZHe
<b>Yan2</b>	Yanggon	102.770	32.228	4269	ZHe
<b>Yan3</b>	Yanggon	102.763	32.224	4612	AFT, ZHe, and ZFT
<b>Yan4</b>	Yanggon	102.760	32.221	4748	AFT and ZHe
<b>Yan5</b>	Yanggon	102.753	32.224	4875	AFT and ZHe
<b>Yan6</b>	Yanggon	102.749	32.222	5000	ZHe
GraA	Sanjiazhai	102.927	32.162	2566	ZHe
GraB	Sanjiazhai	102.894	32.198	3156	ZHe
<b>Mao1</b>	Yanggon	102.945	32.547	3520	AFT and ZHe
<b>Mao2</b>	Yanggon	102.935	32.546	4101	AFT, ZHe, and ZFT
<b>Mao3</b>	Yanggon	102.933	32.553	4224	AFT, ZHe, and ZFT
Lon1	Longriqu	102.643	32.661	3835	AHe, AFT, and ZFT

Note. Bold face indicate samples from the vertical profiles. AHe = apatite (U-Th)/He; AFT = apatite fission tracks; ZHe = zircon (U-Th)/He; ZFT = zircon fission tracks.

**Table 2**  
*Fission Track Data*

Method	Sample	$N_{\text{crystals}}$	$\rho_d (10^6)$	$N_d$	$\rho_s (10^6)$	$N_s$	$\rho_i (10^6)$	$N_i$	Age (Ma $\pm 1\sigma$ )	$P(\chi^2)$ (%)	$D_{\text{par}}$ (range, $\mu\text{m}$ )
AFT	YanA	6	0.98	8,051	0.09	33	1.72	637	6.9 $\pm$ 1.4	13.3	1.41 (1.26–1.50)
	Yan3	8	0.98	8,051	0.03	14	0.73	304	6.2 $\pm$ 1.9	35.8	1.60 (1.45–1.74)
	Yan4	11	0.98	8,051	0.17	110	1.66	1,062	12.9 $\pm$ 1.4	56.4	1.41 (1.09–1.79)
	Yan5	6	0.98	8,051	0.08	30	1.38	501	8.0 $\pm$ 1.5	80.8	1.42 (1.22–1.52)
	Mao1	20	0.98	8,051	0.26	308	1.76	2,076	19.4 $\pm$ 1.6	6.5	1.49 (1.17–1.73)
	Mao2	20	0.98	8,051	0.46	587	1.86	2,352	33.0 $\pm$ 2.2	5.4	1.49 (1.29–1.65)
	Mao3	11	0.98	8,051	0.28	176	0.11	699	37.1 $\pm$ 5.2	1.1	1.43 (1.26–1.63)
	Lon1	17	1.46	8,045	0.21	188	1.02	897	36.5 $\pm$ 3.7	38.1	1.32 (1.11–1.64)
ZFT	Yan3	6	0.41	6,907	8.24	643	3.47	271	61.7 $\pm$ 4.9	58.2	—
	Mao2	5	0.41	6,907	8.66	460	2.92	155	76.8 $\pm$ 7.6	16.9	—
	Mao3	13	0.41	6,907	6.80	1519	2.01	449	87.8 $\pm$ 5.6	18.6	—
	Lon1	7	0.29	8,064	14.50	663	3.07	140	90.0 $\pm$ 8.8	61.1	—

Note.  $\rho_d$  = monitor track density (tracks/cm<sup>2</sup>);  $\rho_s$  = spontaneous tracks density (tracks/cm<sup>2</sup>);  $\rho_i$  = induced fission tracks density (tracks/cm<sup>2</sup>);  $N_d$  = number of tracks counted on the dosimeter;  $N_s$  = number of spontaneous tracks;  $N_i$  = number of induced tracks;  $N_{\text{crystals}}$  = number of counted crystals;  $P(\chi^2)$  = probability to obtain chi square for n degree of freedom ( $n$  = number of crystals-1);  $D_{\text{par}}$  = the mean fission track etch pit diameter.

**Table 3**  
(*U-Th-Sm)/He* Data

	<sup>238</sup> U (mol)	<sup>235</sup> U (mol)	<sup>232</sup> Th (mol)	<sup>147</sup> Sm (mol)	<sup>4</sup> He (mol)	Th (ppm)	Sm (ppm)	eU <sup>a</sup>	Uncorrected age (Ma)	Fl <sup>b</sup>	Corrected age (Ma) <sup>c</sup>	Mean age ± 1SD <sup>d</sup> (Ma)
<b>AHe</b>												
<b>Lon</b>												
Lon1a	547E-14	4.02E-16	3.32E-14	4.60E-15	1.07E-15	8.5	5.0	82.2	13.3	0.68	19.7	21.8 ± 14.5
Lon1b	1.21E-14	8.90E-17	5.21E-15	7.21E-16	1.06E-16	7.7	3.2	39.5	8.4	6.2	0.72	8.5
Lon1c	5.83E-14	4.28E-16	3.87E-14	5.35E-15	8.92E-16	12.9	8.3	89.8	14.8	10.3	0.62	16.7
Lon1d	1.30E-13	9.55E-16	1.01E-13	1.40E-14	6.10E-15	12.8	9.7	104.9	15.1	30.7	0.72	42.3
<b>ZHe</b>												
<b>Gra</b>												
GraA1	2.29E-11	1.68E-13	4.35E-12		2.03E-12	532.0	98.5	555.7	65.4	0.79	82.4	74.1 ± 15.2
GraA2	2.17E-11	1.60E-13	3.80E-12		1.94E-12	625.8	106.8	651.5	66.2	0.79	83.3	
GraA3	1.84E-11	1.35E-13	2.87E-12		1.12E-12	400.4	61.0	415.1	45.4	0.80	56.5	
<b>GraB</b>												
GraB1	1.42E-11	1.04E-13	2.13E-12		5.52E-13	487.6	71.3	504.7	29.1	0.76	38.0	
GraB2	1.72E-11	1.27E-13	2.91E-12		8.83E-13	394.2	63.2	399.3	38.1	0.80	47.7	
GraB3	1.63E-11	1.20E-13	2.85E-12		8.41E-13	520.2	88.7	541.5	38.2	0.77	49.4	
GraB4	1.21E-11	8.86E-14	2.33E-12		8.21E-13	372.9	70.0	389.7	50.1	0.75	66.4	
<b>Yan</b>												
Yan1a	3.11E-11	2.29E-13	4.73E-12		2.57E-12	787.5	116.4	815.4	61.3	0.79	77.4	78.1 ± 6.60
Yan1b	4.75E-11	3.49E-13	7.31E-12		4.33E-12	1,033.6	155.2	1,070.9	68.0	0.80	85.0	
Yan1c	2.44E-11	1.79E-13	3.49E-12		1.86E-12	625.9	87.3	646.9	58.8	0.79	72.0	
<b>Yan2</b>												
Yan2a	1.62E-11	1.19E-13	1.07E-11		1.39E-12	572.5	370.0	661.3	57.2	0.76	74.9	
Yan2b	2.28E-11	1.68E-13	8.88E-12		1.55E-12	481.8	184.5	528.0	48.5	0.80	60.6	
Yan2c	1.13E-10	8.29E-13	1.46E-11		4.93E-12	2,355.7	296.7	2,426.9	32.7	0.80	41.1	
Yan2d	7.91E-11	5.81E-13	1.20E-11		3.32E-12	2,796.0	413.5	2,895.2	31.3	0.76	41.4	87.5 ± 16.2
<b>Yan3</b>												
Yan3a	8.96E-12	6.58E-14	2.00E-12		8.83E-13	553.8	120.5	582.7	72.1	0.74	97.3	
Yan3b	1.63E-11	1.20E-13	3.01E-12		1.59E-12	999.4	179.7	1,042.5	71.8	0.74	96.3	
Yan3c	1.13E-11	8.32E-14	1.57E-12		7.41E-13	369.3	50.0	381.3	48.9	0.71	68.8	
<b>Yan4</b>												
Yan4a	1.08E-11	7.96E-14	3.49E-12		1.92E-12	127.3	105.1	152.5	126.5	0.80	158.3	
Yan4b	3.59E-11	2.63E-13	5.85E-12		3.58E-12	1,312.1	208.8	1,362.2	74.0	0.75	98.4	128.4 ± 4.0
Yan4c	3.66E-11	2.69E-13	2.38E-12		2.24E-12	2,240.6	142.3	2,274.8	46.5	0.75	61.7	
<b>Yan5</b>												
Yan5a	3.75E-11	2.75E-13	1.70E-12		1.57E-12	1,417.3	61.6	1,432.1	32.1	0.75	42.6	
Yan5b	1.57E-11	1.15E-13	2.23E-12		1.60E-12	519.7	70.2	536.6	75.9	0.77	98.1	
Yan5c	2.80E-11	2.06E-13	1.74E-12		2.21E-12	1,134.1	66.8	1,150.1	60.0	0.76	78.9	
Yan5d	8.65E-12	6.35E-14	2.27E-12		8.01E-13	418.8	104.3	443.8	67.3	0.76	88.0	
Yan5e	3.74E-11	2.75E-13	3.27E-12		2.69E-12	1,654.4	141.2	1,688.3	54.3	0.75	72.2	
<b>Yan6</b>												
Yan6a	3.78E-11	2.78E-13	8.01E-12		3.04E-12	1,456.4	300.5	1528.5	59.1	0.76	78.0	91.4 ± 3.0
Yan6b	5.81E-11	4.27E-13	6.49E-12		6.07E-12	704.5	76.8	723.0	78.3	0.83	93.8	
Yan6c	2.34E-11	1.72E-13	2.25E-12		2.08E-12	921.5	86.3	942.2	67.1	0.75	89.0	
Yan6d	5.76E-11	4.23E-13	4.83E-12		3.55E-12	2,021.8	165.2	2,061.5	46.6	0.77	60.7	
<b>Mao1</b>												
Mao1a	1.66E-11	1.22E-13	1.31E-12		2.63E-12	683.6	50.0	695.6	119.1	0.75	157.3	117.2 ± 35.6
Mao1b	8.75E-12	6.48E-14	3.76E-12		9.91E-13	360.8	147.4	396.2	79.3	0.75	105.3	
Mao1c	1.27E-11	9.35E-14	2.31E-12		1.17E-12	634.9	109.7	661.2	68.2	0.76	89.2	
<b>Mao2</b>												
Mao2a	2.01E-11	1.48E-13	3.13E-12		1.67E-12	684.3	99.1	708.1	61.7	0.77	80.0	
Mao2b	9.51E-12	6.99E-14	1.87E-12		9.19E-13	293.5	54.9	306.7	71.1	0.78	91.3	
Mao2c	3.32E-11	2.44E-13	1.02E-11		4.22E-12	958.8	279.9	1,025.9	91.3	0.78	117.1	
Mao2d	2.76E-11	2.03E-13	2.69E-12		2.28E-12	764.6	70.8	781.6	62.1	0.79	78.9	
<b>Mao3</b>												
Mao3a	1.60E-11	1.18E-13	2.74E-12		1.84E-12	655.3	106.3	680.8	84.6	0.75	111.9	119.3 ± 14.7
Mao3b	1.86E-11	1.37E-13	2.98E-12		2.09E-12	690.6	105.0	715.8	83.3	0.76	108.7	
Mao3c	3.93E-12	2.89E-14	1.51E-12		4.90E-13	151.7	55.3	165.0	88.0	0.76	115.8	
Mao3d	1.25E-11	9.21E-14	3.63E-12		1.89E-12	821.9	225.9	876.1	108.3	0.77	141.0	

<sup>a</sup>eU is the effective uranium concentration. <sup>b</sup>Fl is the geometric correction factor for age calculation. <sup>c</sup>Corrected age is the age corrected by the grain geometry and ejection factor Fl. <sup>d</sup>SD is standard deviation. <sup>e</sup>Relected zircon grains (eU<sup>a</sup> > 1400 ppm above which ages are a bit too young).